Nanoscale

Accepted Manuscript

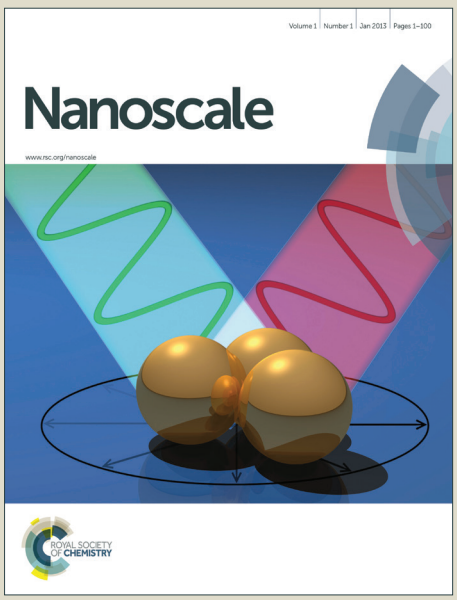

ROYAL SOCIETY OF CHEMISTRY

www.rsc.org/nanoscale

Cite this: DOI: 10.1039/c0xx00000x

www.rsc.org/xxxxxx

Review

Graphene-based hybrid structures combined with functional materials of ferroelectrics and semiconductors

Wenjing Jie[ab] and Jianhua Hao[ab*]

Received (in XXX, XXX) Xth XXXXXXXXX 20XX, Accepted Xth XXXXXXXXX 20XX

DOI: 10.1039/b000000x

Fundamental studies and applications of 2-dimentional (2D) graphene may be deepened and broadened via combining graphene sheets with various functional materials, which have been extended from traditional insulator of SiO_2 to a versatile range of dielectrics, semiconductors, metals as well as organic compounds. Among them, ferroelectric materials have received much attention due to their unique ferroelectric polarization. As a result, many attractive characteristics can be shown in graphene-ferroelectric hybrid system. On the other hand, graphene can be integrated with conventional semiconductors and some newly-discovered 2D layered materials to form distinct Schottky junctions, yielding fascinating behaviours and exhibiting the potential for various applications in future functional devices. This review article is an attempt to illustrate the most recent progress on the fabrication, operation principle, characterization, and promising applications of graphene-based hybrid structures combined with various functional materials, ranging from ferroelectrics to semiconductors. We focus on mechanically exfoliated and chemical-vapor-deposited graphene sheets integrated in numerous advanced devices. Some typical hybrid structures have been highlighted, aiming at the potential applications in non-volatile memories, transparent flexible electrodes, solar cells, photodetectors, and so on.

1. Introduction

Two-dimensional (2D) material is formed when one dimension is restricted in size. In general, 2D materials are expected to exhibit unique properties that are substantially different from their bulk materials, thus making them attractive from both scientific and technological viewpoints. Graphene is a carbon layer that consists of a honeycomb lattice structure, which was firstly discovered by mechanical exfoliation using adhesive tapes by Geim's group at Manchester University in 2004.[1] The specific definition of graphene is a single-atom-thick sheet of hexagonally arranged, sp2-bonded carbon atoms that is not an integral part of a carbon material, but is freely suspended or adhered on a foreign substrate.[2] Graphene is a semi-metal with zero bandgap. Its valence and conduction bands are cone-shaped and meet at the *K* points of the Brillouin zone. With its unique 2D-layered structure, graphene exhibits outstanding electronic, thermal, optical, and mechanical properties.[3,4] 2D materials are essentially capable of presenting unusual optical and electronic properties due to the confinement of electrons as well as the absence of interlayer interactions. Some other changes in properties, such as mechanical and chemical response, are mainly due to the geometry effects and to the high surface-bulk ratio. Single-layer graphene has a large theoretical specific surface area (~2630 m^2g^{-1}), high intrinsic mobility (room temperature reaching 200 000 cm^2 $v^{-1}s^{-1}$),[5] and low electrical conductivity,[6,7] good impermeability (gas and liquid),[8,9] excellent thermal conductivity (~5000 $W^{-1}K^{-1}$),[10] low absorption in white light spectrum (~2.3%),[11] and high Young's modulus (~1.0 TPa).[12] Accordingly, graphene has been explored in a wide range of applications, such as optoelectronics, spintronics, sensors, supercapacitors, solar cells and so on.[13,14]

In general, 2D graphene sheets need to be combined with some other bulk or thin film materials, mainly providing mechanical support. Furthermore, those combined functional materials may play important roles in improving the intrinsic properties of graphene sheets or even ascribing additional features to graphene sheets. Graphene exhibits versatile electronic and photonic properties when integrating with different functional materials due to significant surface or/and interface effects of various hybrid structures. Therefore, graphene-based heterostructure devices can be constructed via selecting appropriate functional materials. Furthermore, understanding and utilizing the impacts of functionalities on graphene and the overall hybrid system are critical to fully achieving the fundamental and technological potential of graphene. The first graphene-based device, reported by Novoselov et al. in 2004,[1] was made by integrating graphene with silicon to form field-effect transistor (FET), in which several-hundred-nanometer SiO_2 was employed as an insulating layer (gate layer) to provide an external electric field to graphene. Currently, graphene has already been considered to be one of the most promising materials for future applications in nanoelectronics.[15,16] To date, not only the gate type has been developed from back-gated to top-gated or dual-gated, but also the gate material of SiO_2 has been partially substituted by other dielectrics, such as HfO_2, Al_2O_3, $SrTiO_3$, etc. The graphene-based hybrid systems have

been explored to a wide variety of potential applications, including electronic, photonic and optoelectronic components and devices. And the materials integrated with graphene are also expanded from traditional oxides to a versatile range of functional dielectrics and semiconductors.

Among functional dielectrics, ferroelectrics not only possess high dielectric constant and nonlinearlity,[17–20] as well as optical characteristics,[21–24] but also exhibit non-volatile memory behaviours due to their unique feature of spontaneous polarization.[25,26] This enables ferroelectrics to be suitable for high-density capacitors, tunable microwave components, multifunctional devices, and non-volatile memories. Integrating graphene with ferroelectrics can introduce non-volatile doping to graphene. Additionally, it is interesting to find that the conductivity and mobility of graphene could be enhanced by the ferroelectric polarization,[27,28] yielding a promising application in flexible transparent conductors for graphene/ferroelectric hybrid systems.[27,29] Although many research groups have paid much attention on such hybrid systems, few articles have given a critical review on this specific heterostructure consisting of graphene and ferroelectric materials. On the other hand, graphene, as a semi-metal, can somewhat serve as a metal active layer to form metal-semiconductor (M-S) Schottky contact with some semiconductors, such as Si, SiC, GaAs, GaN and graphene oxide etc,[30–35] if the work function difference between graphene and the semiconductor is large enough, and the carrier density of the later is moderate.[36] Especially, a number of 2D semiconductors beyond graphene have been discovered, and therefore, the combination of graphene with those 2D semiconductors can result in the formation of Schottky junctions with vertical thickness at nanoscale. Consequently, such M/S diodes based on the graphene/semiconductor hybrid systems may find many promising applications, such as photodetectors, solar cells and so on. In this review paper, we will introduce various hybrid systems combining graphene with functional materials, ranging from ferroelectrics to semiconductors. Some aspects of system fabrication, working principle and characterizations of various devices will be discussed. We will highlight some important progress in developing novel nanoscale devices based on graphene-functional materials hybrid structures, including non-volatile memories, transparent flexible electrodes, solar cells, and photodetectors.

2. Constituent and formation of the hybrid system

2.1 Preparation of graphene

As of now, versatile methods have been developed to grow or synthesize graphene sheets. Firstly, mechanical exfoliation of highly oriented pyrolytic graphite is a convenient way to obtain the pristine graphene with high quality. Micro-scale graphene flakes can be cleaved and adhered to the subsequent target substrate,[1] as shown in Fig. 1(a) and (b) of the optical and atomic force microscopy (AFM) images of graphene on oxidized Si substrate, respectively. The layer number of mechanically exfoliated graphene can be identified by measuring the thickness of such flakes. Furthermore, the layer number of graphene can be determined by using optical microscopy in normal white light according to the color of it with an optimized thickness of the underlying SiO_2. Generally, the size of such graphene sheets is limited and it is difficult to achieve wafer-scale graphene by such a method. However, mechanical exfoliation is a simple and cost-effective way to get high-quality but small-sized graphene at micro-scale.

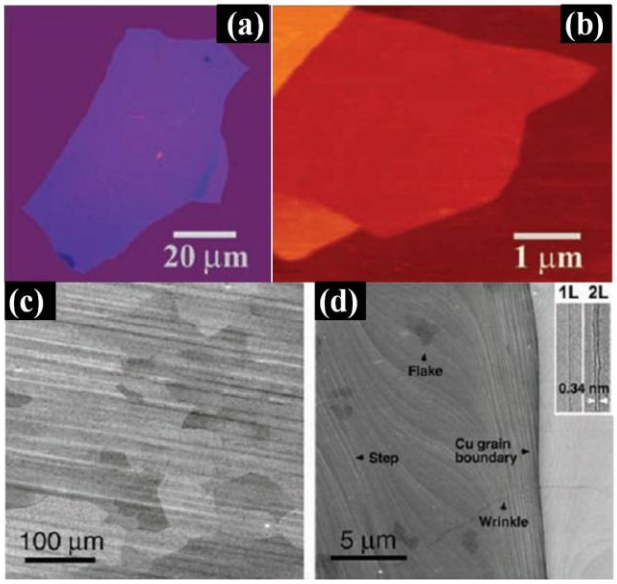

Fig. 1 The characterization of the mechanically exfoliated and CVD-grown graphene by different microscopy techniques. (a) Optical and (b) Atomic force microscopy image of mechanically exfoliated multilayer graphene on oxidized Si wafer. Reproduced with permission from ref. 1. Copyright 2004 American Association for the Advancement of Science. (c) Scanning electron microscopy (SEM) image of CVD-grown polycrystalline graphene on copper sheet. (d) High-resolution SEM image clearly showing the copper grain boundaries and graphene wrinkles. The inset in (d) shows the transmission electron microscopy (TEM) image of single-layer (1L) and bilayer (2L) folded graphene edges. Reproduced with permission from ref. 38. Copyright 2009 American Association for the Advancement of Science.

It is known that high-quality and large-area graphene is required, facilitating manipulation and integration into complex devices suitable for electrical and optical applications. In this sense, the bottom-up growth of graphene sheets, as an alternative to the mechanical exfoliation, is an essential technique. Chemical vapor deposition (CVD) has been employed to grow large-area graphene sheets on metal surfaces, such as Ni and Cu.[37,38] However, CVD-grown graphene are typically polycrystalline composing of many domain boundaries and graphene wrinkles. Fig. 1(c) and (d) show the scanning electron microscopy (SEM) and high-resolution SEM images of graphene on Cu sheet, respectively.[38] The Cu grain boundaries and graphene wrinkles are clearly visible. In spite of the presence of Cu surface steps, graphene wrinkles, and non-uniform dark flakes, large-area polycrystalline graphene sheet can be successfully grown on Cu as well as Ni substrates.

One challenge, also a fundamental step in fabricating graphene-based hybrid system, is to transfer thin flakes from metal substrates to some pre-defined substrates without damaging

graphene or degrading the graphene properties. The conventional transfer process can be performed by spin coating a layer of organic polymer, such as poly(methyl methacrylate) (PMMA) or polydimethylsiloxane (PDMS), on the top surface of graphene as a mechanical supporting layer. Then, the initial underlying metal substrates (Ni or Cu) are etched by particular solutions to obtain the suspended graphene with the help of the above PMMA supporting layer. After that, the PMMA/graphene membrane can be placed onto the target substrate and the above PMMA layer can be dissolved with acetone after transferring graphene onto the target substrate. Besides for that, some transfer techniques have been developed to realize in combining graphene with an arbitrary substrate. Kim et al reported a dry-transfer method using a soft substrate of PDMS stamp to transfer pre-patterned graphene with various size and shape.[37] Bae et al proposed a roll-to-roll transfer method which can transfer 30-inch graphene films from copper sheet onto plastic substrate with a polymer support.[39] Besides, millimeter-sized single-crystal graphene sheets can be grown on Pt substrate by ambient-pressure CVD technique. A bubbling method was employed to transfer these single-crystal graphene sheets to arbitrary substrate. This approch is essentially nondestructive not only to graphene, but also to Pt substrate.[40]

Additionally, graphene has also been synthesized by the desorption of Si from SiC single-crystal surfaces, which yields a multilayered graphene,[41] by a surface precipitation process of carbon in some transition metals,[42] by chemical reduction of graphene oxide to produce covalently functionalized single-layer graphene,[43] and by chemical exfoliation.[44,45] In this review, we focus mainly on the use of mechanically exfoliated pristine graphene and CVD-grown large-area poly-crystalline graphene to form hybrid systems.

2.2 Selection of functional materials

A combination of graphene with various functional materials may bring great impacts to the graphene layer, and hence significantly broaden the spectrum of graphene applications. SiO_2 is the first and extensively investigated material integrated with graphene. Subsequently, graphene flake has been combined with various types of functional materials, ranging from inorganic high dielectrics (HfO_2, $SrTiO_3$, and $PbZrTiO_3$, etc.), semiconductors (Si, GaAs, etc.), metals, to organics and stretchable polymers. Very recently, integrating graphene with some graphene-like 2D materials has also drawn much attention.

Note that one of most useful dielectrics, namely ferroelectrics can exhibit a spontaneous polarization which is switchable via an external electric field. The polarization of the ferroelectric oxide is typically one order of magnitude higher than what can be induced through conventional SiO_2 gate. In principle, there are 32 crystalline classes which have been found in crystals, in which there are 21 non-centrosymmetric classes, corresponding to piezoelectric. Among the piezoelectric classes, 10 classes so-called pyroelectric have spontaneous electric polarizations varying with the temperature. Some of pyroelectric materials belong to ferroelectric, and therefore, ferroelectric materials possess not only the spontaneous and switchable polarizations, but also the properties of pyroelectricity and piezoelectricity. And such fascinating properties enable ferroelectrics to show many practical applications, as shown in Fig. 2. When graphene is incorporated with ferroelectric materials, the hybrid system also exhibits amazing behaviours, such as non-volatility, lower sheet resistivity, higher mobility in non-suspended graphene, as well as the strain effects induced by the piezoelectricity and additional polarization effects caused by the pyroelectricity.

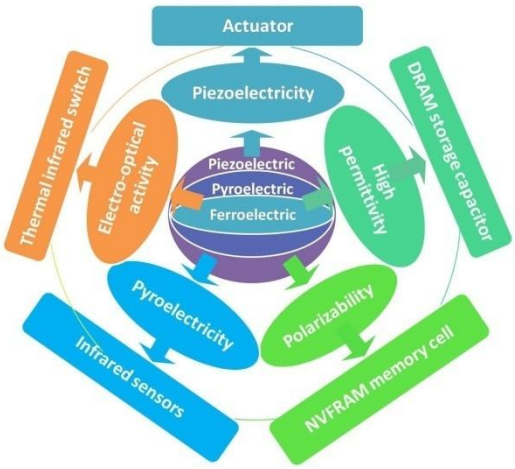

Fig. 2 Various properties of ferroelectric materials and the potential applications.

On the other hand, semiconductors, as the dominated materials in modern electronics and optoelectronics, have a number of useful properties. Typically, electrical conductivity of semiconductors can be readily changed by doping impurities or excitation of stimuli, such as electric field or photon. As a consequence, modern electronic and optoelectronic devices are built using a range of semiconductors along with insulators and metals. Graphene as a semi-metal can be incorporated with some n-type traditional semiconductors with moderate carrier density to form a Schottky junction. Besides, a large variety of graphene-like 2D materials can be exfoliated from some layered materials with the stacked structure in their bulk materials like graphite. Among them, transition metal dichalcogenides (TMDCs), consisting of hexagonal layers of transition metal atoms (M, typically Mo, W, Nb, Re, Ni, or V) and sandwiched between two layers of chalcogen atoms (X, typically S, Se, or Te)) with a MX_2 stoichiometry (like MoS_2, WS_2, etc.), show a big category in 2D family. Those newly discovered 2D materials are intrinsically semiconductors, which have the potential to be integrated with graphene sheets. Based on the single-junction diode, graphene/semiconductor hybrid systems have received much attention in view of their promising applications for future nano-electronics or nano-optoelectronics.

3. Hybrid system between graphene and ferroelectrics

Recently, organic and inorganic ferroelectric materials have been employed in graphene-based FETs as gate dielectrics for memory applications.[28,46–49] The non-volatile memory based on graphene/ferroelectric has drawn much attention, and, the investigated ferroelectric materials used in hybrid system range

from inorganic lead zirconate titanate (PZT) and (1-*x*)[$Pb(Mg_{1/3}Nb_{2/3})O_3$]-*x*[$PbTiO_3$] (PMN-PT) to organic ferroelectric poly(vinylidene fluoride-co-trifluoroethylene) (PVDF-TrFE). Interestingly, the combination of low-resistance graphene on stretchable PVDF-TrFE is promising for flexible electronic applications. Additionally, with the piezoelectric properties in ferroelectric materials, it becomes feasible to investigate controllable biaxial strain effects on graphene by coupling piezoelectric effect to graphene. Apart from these effects, the pyroelectric behaviours existed in ferroelectric materials may provide an opportunity to develop graphene based photodetectors.

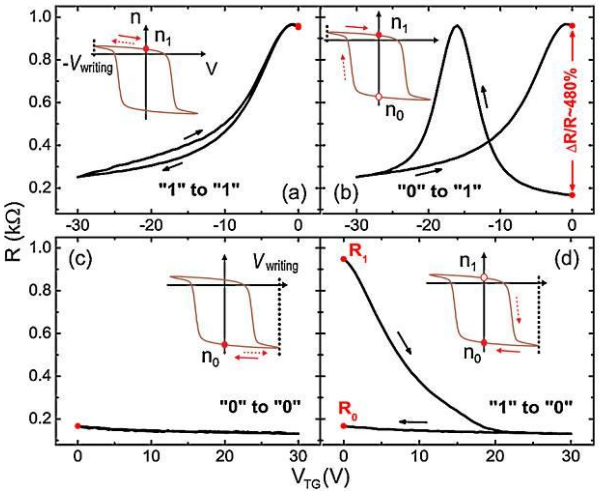

Fig. 3 The writing process of non-volatile memory based on graphene/ferroelectric hybrid system. Symmetrical bit writing (a) from "1" to "1"; (b) from "0" to "1" by using the negative writing voltage ($-V_{writing}$); (c) from "0" to "0"; (d) from "1" to "0" by using the positive writing voltage ($V_{writing}$). Reproduced with permission from ref. 48. Copyright 2010 American Physical Society.

3.1 Non-volatile memories

The device state of non-volatile memory is determined by the writing voltage ($V_{writing}$) rather than the initial state. To be more specific, when the $V_{writing}$ is negative, the FET shows high-resistance state "1", regardless of the initial state of the FET, as shown in Fig. 3(a) and (b).[46,48] In contrast, a positive $V_{writing}$ with the same magnitude can set the unit cell into low-resistance state "0". Fig. 3(c) and (d) indicate the graphene/ferroelectric hybrid system can achieve the bit writing of "0" from "0" and "1", respectively. So, the writing state is independent on the initial states and is only determined by the $V_{writing}$. Generally, the ferroelectrics integrated in FETs include PZT thin films, organic PVDF-TrFE, and PMN-PT single crystals, while both mechanically exfoliated and CVD-grown graphene sheets are used in non-volatile memories.

3.1.1 Mechanically exfoliated graphene.

Few-layer graphene (FLG) sheets were ever integrated with ferroelectric PZT epitaxial thin film grown on Nb-doped $SrTiO_3$ (STO) substrate via radio-frequency magnetron sputtering by Zhu et al.[28] Fig. 4(a) shows AFM and optical images of the graphene sheets on 300 nm thick PZT thin films.[47] The schematic of the hybrid system of graphene/PZT is shown in Fig. 4(b). The PZT thin films served as the gate oxide to substitute traditional SiO_2 to form FETs. The source and drain electrodes were prepared by standard lithography technique. Nb-doped STO substrate served as a bottom electrode, where the gate voltage (V_g) was applied on PZT to tune the carrier density of the above graphene layers. When the applied V_g is sufficiently large, the system becomes completely electron-contributing and the electron density is calculated to be about 1.5×10^{12} cm^{-2}. The temperature-dependent sheet resistivity of FLG on PZT thin film demonstrates a mobility in excess of 1.5×10^5 cm^2 V^{-1} s^{-1}, which was the highest reported mobility to that date in unsuspended single- and few-layer graphene devices. Therefore the ferroelectric gating opens up a new route for making integrated graphene-based FETs to realize high-speed electronic devices.

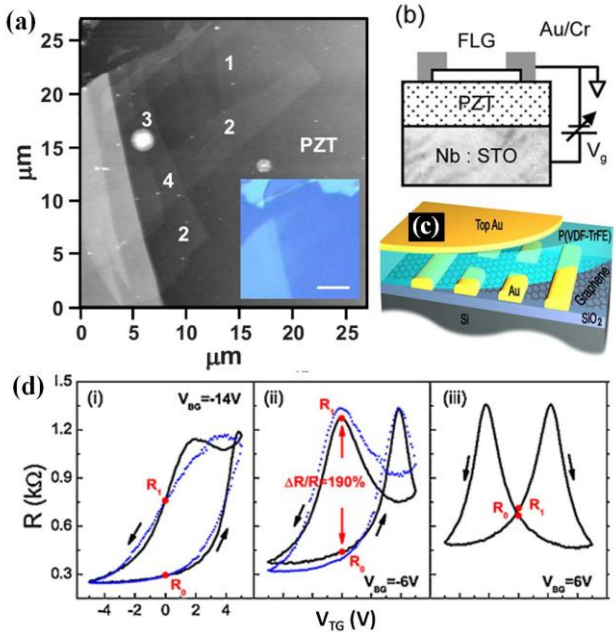

Fig. 4 The mechanically exfoliated graphene integrated with PZT and PVDF for memory applications. (a) AFM image of a multilayer graphene sheet on PZT thin film with the thickness of about 300 nm. The height measurements of the sheets can be used to determine the layer numbers and marked in the figure. Inset shows the optical image of the same graphene sheet. The scale bar is 10 μm. Reproduced with permission from ref. 47. Copyright 2010 American Institute of Physics. (b) Schematic of the hybrid system between graphene and PZT. Reproduced with permission from ref. 28. Copyright 2009 American Physical Society. (c) Schematic of the hybrid system of P(VDF-TrFE)/graphene/SiO_2. (d) The dependence of R on the V_{TG} with different V_{BG}. The blue dotted lines are simulated results. Reproduced with permission from ref. 48. Copyright 2010 American Physical Society.

The non-volatile memory based on graphene/ferroelectric hybrid system was ever made by Özyilmaz et al. The organic ferroelectric of PVDF-TrFE polymer was utilized as a top gate to functionalize the graphene-based FETs, while normal SiO_2 served as both bottom gate and substrate, providing independent

background gating and mechanical support, respectively.[46,48] The geometry of this hybrid system is shown in Fig. 4(c), and the thickness of the ferroelectric PVDF is about 500 nm. The electrical properties of FETs are characterized at room temperature in vacuum. Compared to traditional SiO_2 gating, one fundamental difference introduced by ferroelectric gating is the hysteresis in the resistance of graphene can be produced as a function of top gate voltage (V_{TG}). By using the SiO_2 as bottom gate, an independent bottom gate voltage (V_{BG}) could be generated to provide a well-defined and constant reference to PVDF, and also the doping level and carrier density of graphene could be modified by the bias voltage. The curves of resistance (R) as function of V_{TG} under different V_{BG} were measured, as shown in Fig. 4(d). The V_{TG} applied on PVDF is relatively low, only slightly polarizes the PVDF, to ensure the V_{TG}-induced carrier density is comparable to the V_{BG}, considering the ferroelectric gating is nearly 10 times stronger than the SiO_2 gating.[46] At relatively high bias voltage applied to PVDF (for example, ± 30 V), the ferroelectric polarization can be switched in the unit cell. Additionally, the fatigue test shows that reproducible non-volatile switching exceeding 100 k cycles in this unit cell, suggesting a cost-effective solution for flexible non-volatile data storage. Thus, by using such dual-gated PVDF/graphene/SiO_2 hybrid system, the independent dielectric gating can be used to control ferroelectric gating, and more importantly, in such hybrid system, symmetrical bit writing can be functionalized to realize the non-volatile memory.

Besides, Raghavan et al proposed a PVDF-gated-graphene-based FET unit cell, with similar hybrid structure, exhibiting long-term retention performance for both memory states.[50] Both high and low resistance states were reported to reach saturated after 25 h and then remain unchanged for the subsequent 50 h with a factor of difference of 2.5 between the two resistance states.

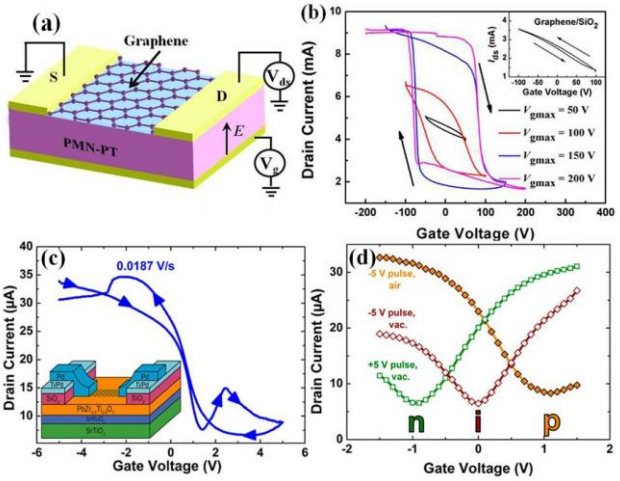

Fig. 5 The CVD-grown graphene integrated with PMN-PT and PZT for memory applications. (a) Schematic of graphene/PMN-PT hybrid system (b) I_{ds}–V_g curves of graphene on the PMN-PT with different initial sweeping voltage from 50 to 200 V. Inset: I_{ds}–V_g curves of graphene on the SiO_2. Reproduced with permission from ref. 53. Copyright 2013 American Chemical Society. (c) Complex I_{ds}–V_g characteristics of graphene on single-crystal PZT thin film prepared by sputtering on $SrTiO_3$ substrate. Inset: Schematic of a graphene/PZT hybrid system on $SrTiO_3$ substrate. (d) The transport characteristics of graphene with the V_g not exceeding the coercive voltage measured after a pulse voltage of ± 5 V. Reproduced with permission from ref. 52. Copyright 2013 American Chemical Society.

3.1.2 Chemical-vapor-deposited graphene.

The operation principle of the non-volatility based on graphene/ferroelectric hybrid systems has been further explored for both mechanically exfoliated and CVD-grown graphene.[51,52] Recently, our group also integrated the hybrid system between CVD-grown single-layer graphene (SLG) with ferroelectric PMN-PT single crystal with the thickness of 0.5 mm, as schematically shown in Fig. 5(a).[53] The characterization of this hybrid system was performed at the room temperature in air. The V_g-dependent drain-source current (I_{ds}) shows that graphene/PMN-PT FET is p-type with a large memory window for the maximum sweeping voltage V_{gmax} in excess of 100 V [Fig. 5(b)]. Generally speaking, the graphene usually shows p-type characteristics in air at room temperature[54,55] However, n-type graphene or the reduction of p-doping is still desirable.[56,57] In our experiments, by pre-poling the PMN-PT substrate, the FET showed a reduction in p-doping for the graphene/PMN-PT FET.

Moreover, Baeumer et al transferred CVD-grown SLG onto pulsed-laser deposition grown ferroelectric PZT thin film with thickness of 140 nm on STO substrate with a $SrRuO_3$ layer as bottom electrode, in order to form graphene/PZT FETs [Fig. 5(c)].[52] Ferroelectric polarization arising from the underlying PZT thin film was proposed to be effectively switched using the top graphene electrode, while such polarization also could control the carrier type and density in graphene based FETs. As shown in Fig. 5(d), the carrier type of graphene can be tuned from initial p- to eventual n-type by 1 ms pulse of gate voltage before the measurement, indicating a strong influence of ferroelectric polarization on the electronic properties of graphene. The initial pulse voltage applied to the PZT, which is larger than the coercive voltage, can completely switch the polarization, and such a state can be retained. As a consequence, a complete reversal in vacuum condition can be obtained from p-type into n-type graphene by a pre-applied pulse voltage.

Furthermore, Song et al carefully compared mechanically exfoliated and CVD-grown SLG sheets on PZT thin films with the optimal thickness of 180 nm deposited on Pt/Ti/SiO_2/Si substrates [Fig. 6(a)].[51] For exfoliated graphene, shown in the top graph of Fig. 6(b), the FET exhibits large memory window which is nearly equivalent to the hysteresis of the PZT thin film. Compared to the exfoliated one, the main difference for CVD-grown graphene is the initial doping level due to the etchant solution during the process of removing the underlying Cu sheets.[58] Such effects give rise to the distinct hysteresis behaviours compared to exfoliated graphene. Besides, the curve of drain current (I_d) vs V_g has an opposite direction from the polarization direction of the underlying ferroelectric material, which has also been reported in the aforementioned references. Such behaviours can be explained by the charge trapping in the interface states and the polarization screening from the water

molecules located on the interface.[47,59]

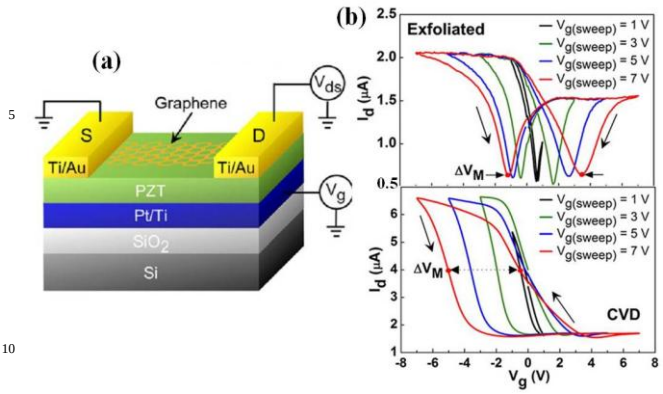

Fig. 6 The comparison between exfoliated and CVD-grown graphene integrated with PZT for memory applications. (e) Schematic of graphene/PZT hybrid system on Pt/Ti/SiO_2/Si substrate. (f) I_{ds}–V_g curves with different sweeping voltage for exfoliated (above) and CVD-grown (bottom) graphene on PZT thin film. Reproduced with permission from ref. 51. Copyright 2011 American Institute of Physics.

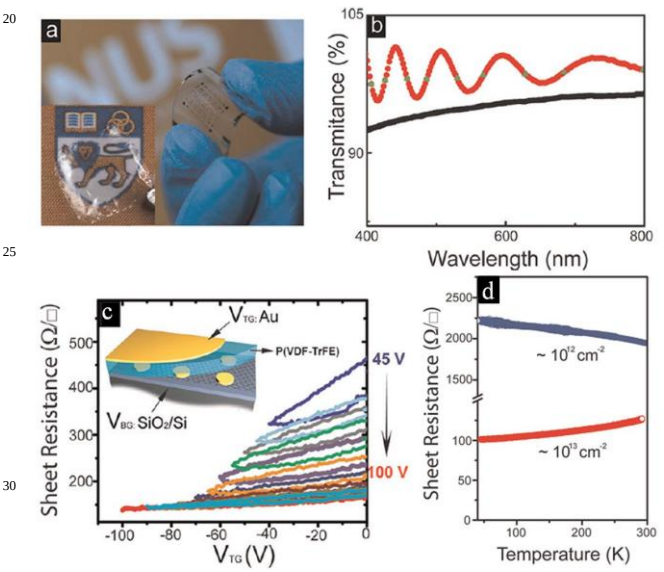

Fig. 7 The CVD-grown graphene integrated with PVDF for flexible electrodes. (a) Optical image of Graphene/PVDF-TrFE thin film on transparent PET substrate. Inset: optical image of a free-standing graphene/PVDF-TrFE thin film; the background is the logo of National University of Singapore. (b) Transmission spectra of graphene/PVDF hybrid structure and pure PVDF-TrFE thin film as a function of wavelength from the visible to near IR range. The red curve shows the optical image of a pure PVDF-TrFE thin film. The vibration of P(VDF-TrFE) is due to the interference effect. (c) V_{TG}-dependent Sheet resistance swept at different V_{TGmax} Inset: Schematic of graphene/PVDF-TrFE hybrid system on SiO_2 substrate. (d) Temperature-dependence R_s of GFeTCs before and after polarization charge density levels. Reproduced with permission from ref. 27. Copyright 2012 American Chemical Society.

3.2 Flexible transparent electrodes

Historically, indium tin oxide (ITO) has widely been used as transparent electrodes because of its high electrical conductivity and good optical transparency. However, ITO is brittle, severely limiting its application to flexible devices. Although graphene has high electrical mobility and conductivity, it still needs to optimize graphene in order to achieve comparable low sheet resistance of ITO as transparent electrodes in practical applications. Some approaches have been used to reduce sheet resistance of graphene. Among them, chemical doping is a traditional method,[60–62] which can generally induce the degradation of conductivity of chemical-doped graphene by the adsorption of moisture and introducing other chemical molecules.[63,64] The ferroelectric polymer of PVDF-TrFE has been exploited as an effective gate material to control the transport properties of graphene, but also shows the mechanical flexibility and optical transparency. The sheet resistance of CVD-grown large-scale graphene can be effectively reduced by employing PVDF-TrFE to fabricate hybrid system for flexible and transparent electrode. [27,29]

The graphene-ferroelectric transparent conductors (GFeTCs) exhibit a low sheet resistance (R_s) of about 120 Ω/squr in air ambient conditions and high transparency (~95%) in the visible wavelength range.[27] For optical and mechanical measurements, GFeTCs are prepared by spin coating about 10 μm PVDF-TrFE on graphene on Cu sheets followed by etching the underlying Cu and transferring PVDF-TrFE/graphene to transparent substrates, such as polyethylene terephthalate (PET). The ferroelectric polymer was employed as dielectric layer as well as mechanical supporting layer in the hybrid structures. As shown in Fig. 7(a) and (b), GFeTCs on PET substrates and free-standing GFeTCs exhibit good optical transparency and mechanical flexibility. The mechanical properties have also been characterized by measuring the resistance of the GFeTCs on PET with respect to bending radius. The measured resistance shows a small increase and can be recovered completely after unbending, which is similar to the results of graphene sheets on stretchable organic substrate.[37,65] For the R_s measurements, GFeTC devices are fabricated by firstly transferring graphene on SiO_2, then preparing metal contacts on the top surface of graphene, after that, spin coating about 10 μm PVDF-TrFE on graphene/SiO_2. The hybrid system is schematically shown in the inset of Fig. 7(c). Prior to fully polarizing the PVDF, the R_s of graphene is about 1440 Ω/squr, while a 12-fold reduction (120 Ω/squr) of R_s is achieved after full polarization of the ferroelectric polymer. The V_{TG}-dependent R_s under different sweeping voltage as shown in Fig. 7(c), indicates lower R_s could be achieved at high negative V_{TG}. Due to the non-volatile doping induced by PVDF-TrFE, sheet resistance of large-scale graphene remains low, even when the power is turned off. Temperature-dependent R_s measurements are shown in Fig. 7(d). GFeTCs show a clear transition from insulating behaviour (low doping, initial un-polarizing) to metallic behaviour (high doping, fully polarizing). The ferroelectric PVDF-TrFE provides non-volatile electrostatic doping, yielding a low sheet resistance, while the ferroelectric polymer does not compromise the high optical transparency of graphene. Furthermore, a sandwich

structure of graphene/PVDF/graphene not only shows good electrical conductivity with R_s of 188 Ω/squr, but also promises to realize transparent and flexible acoustic actuator and nanogenerator.[29]

3.3 Piezoelectric and pyroelectric effects on graphene

3.3.1 Piezoelectricity.

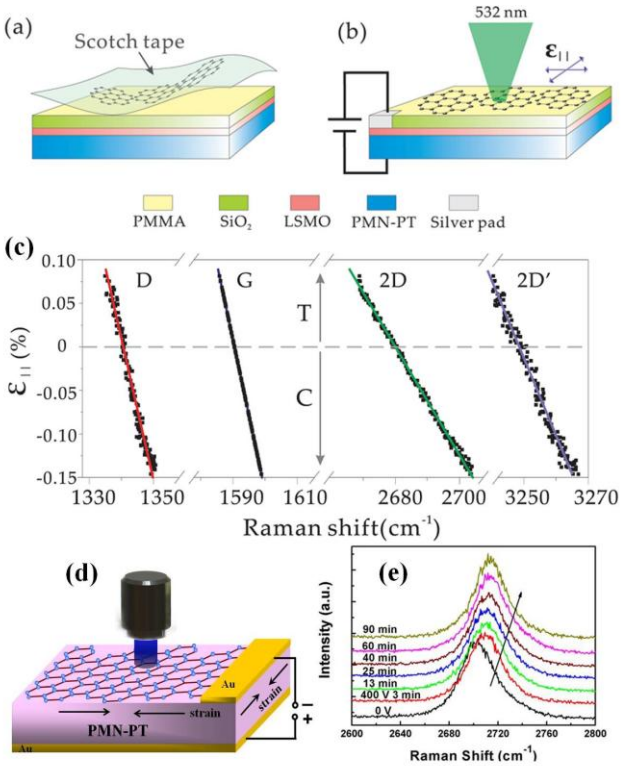

Fig. 8 Strain engineering for the hybrid system of graphene and PMN-PT. (a)Transfer mechanically exfoliated graphene onto PMMA/SiO_2/LSMO covered PMN-PT substrate. (b) Schematic of the piezoelectric actuator by applying perpendicular electric field to provide in-plane biaxial strain to the graphene. (c)The position of D,G, 2D, and 2D' peaks plotted as a function of the in-plain biaxial strain $\varepsilon_{||}$, including both tensile strain (T) and compressive strain (C), and the solid lines are linear fits. Reproduced with permission from ref. 74. Copyright 2010 American Chemical Society. (d) Schematic of CVD-grown graphene/PMN-PT hybrid system by applying perpendicular electric field to provide in-plane biaxial strain to the graphene. (e) The time-dependent 2D peaks of the graphene during the retention of bias voltage of 400 V. Reproduced with permission from ref. 75. Copyright 2013 American Institute of Physics.

In principle, piezoelectricity results from linear interaction between mechanical and electrical systems in non-centric crystals. In the view of the point group, crystals belonging to the point groups with non-centric symmetry are able to produce piezoelectric effect. An internal structure deformation can be induced by an external electric field. For, example, PMN-PT single crystals are excellent piezoelectric materials, possessing high electromechanical coupling coefficients and high electrically induced strains.[25,26,66] These excellent properties of PMN-PT, which are superior to those traditionally used PZT ceramics, have already been considered to develop transducer, actuator and optical applications. It should be noted that the strain provided by the piezoelectric crystal is biaxial strain in nature, and the structure deformation in x axis is always kept same to that in y axis. It has been proven to be feasible to utilize biaxial strain to study the basic vibrational properties of graphene.[67,68] It is a common fact that uniaxial strain can be introduced to graphene simply by stretching or bending the graphene-coated flexible substrates, including PDMS,[65] PMMA,[69] and polyethylene terephthalate (PET)[70,71]. However, such uniaxial strain could cause the shift of the relative positions of the Dirac cones, and further induce significant influence on the double-resonance process of graphene, which is not suitable for investigating the Grüneisen parameters.[72,73]

Ding et al. ever applied biaxial strain caused by PMN-PT to mechanically exfoliated monolayer graphene.[74] Besides, our group also prepared CVD-grown polycrystalline graphene/PMN-PT hybrid system.[75] According to these two published works, tunable strain effects on graphene are studied by applying perpendicular electric field to the piezoelectric substrate of PMN-PT, as schematically shown in Fig. 8(a), (b) and (d). For exfoliated graphene, 40 nm thick epitaxial layer of $La_{0.7}Sr_{0.3}MnO_3$ (LSMO) serves as the electrode when applying bias voltage. The thickness of SiO_2 (1 μm) and PMMA layer (60 nm) were carefully optimized to visualize the graphene layer under an optical microscope. By applying perpendicular electric field, the position of feature peaks for graphene (D, G, 2D and 2D') can be tuned, showing reproducible shift, as shown in Fig. 8(c). The Grüneisen parameters can be calculated according to the shift of feature peaks under biaxial strain. Similar Raman shifts can also be detected by exerting the piezoelectric strain to CVD-grown graphene. Therefore, such novel graphene/piezoelectric hybrid system provides one an opportunity to investigate controllable biaxial strain effect on graphene. Such piezoelectric strain could induce a blue shift under compressive strain, while a red shift under tensile strain. However, for CVD-grown polycrystalline graphene, the strain distribution could be different between the inside of grain and the grain boundary. As a result, the grain boundary existed in graphene may give rise to unexpectable strain effect on the behavior of CVD-grown graphene, as shown in Fig. 8(e). An additional Raman shift of 2D peak can be detected during the retention of the bias voltage.

3.3.2 Pyroelectricity.

The pyroelectric materials are those whose polarization can be changed when the temperature is varied. The pyroelectric FET based on graphene/PZT hybrid system is proposed by utilizing the infrared (IR) laser to generate the thermal energy leading to an increase in the temperature of PZT, as schematically indicated in Fig. 9(a).[76] The carrier in graphene could be converted from electron to hole when the polarization is varied from upward to downward. As a consequence, the drain current can be increased or decreased under the exposure to IR laser corresponding to the upward or downward polarization direction, respectively. This is because the IR-induced thermal energy gives rise to the extra polarization of PZT due to the pyroelectric effects. As a result,

the drain current can be tuned by modulating the IR illumination with a manual light blocker, as shown in Fig. 9(b). In comparison, there is no noticeable change in the drain current under the IR illumination for the graphene/SiO_2 FETs. And more importantly, when the polarization direction is changed, the drain current of the grpahene/PZT FET shows totally converse change, implying that polarization plays a key role in the observed behaviours, ruling out the possibility of high temperature effect on the graphene.

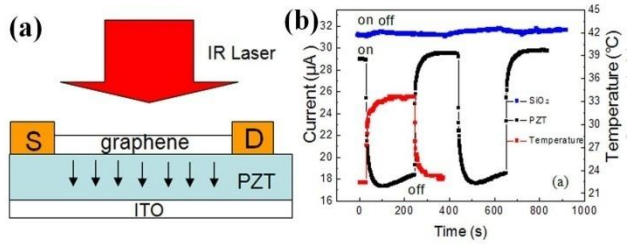

Fig. 9 The hybrid system of graphene and pyroelectric PZT. (a)The schematic the graphene-PZT field effect transistor influent by the incident IR laser. (b)The behavior of current and temperature as a function of time modulated by IR laser of 320 mW corresponding to the downward polarizations of the PZT. Reproduced with permission from ref. 76. Copyright 2012 American Institute of Physics.

4. Hybrid system between graphene and semiconductors

Because of the two-dimensionality and structural flatness, graphene sheets can be considered to be ideal candidates for thin-film devices combined with conventional semiconductors, including silicon, GaAs and so on. The device structures and electrical properties can be determined by the hetero-interface between graphene and those conventional semiconductors. It is well-known that the Fermi energy level of semiconductors can be tuned by impurity doping. On the other hand, the work function of graphene can be modulated by various methods, such as electric field, doping, layer number, etc. Based on the difference of the work-function between graphene and semiconductor, the graphene/semiconductor hybrid devices can be developed. In addition, graphene's excellent electrical and optical characteristics make it suitable for the employment of transparent electrodes in many electronic, optical and optoelectronic devices, including light-emitting diodes (LEDs), photodetectors and solar cells. In fact, so far most reports on LEDs, especially organic LEDs (OLEDs), involved in graphene mainly made use of transparent and conductive characteristics of graphene instead of hetero-interface.[77–79] Ye et al. demonstrated the graphene nanoribbon/semiconductor nanowire heterojunction LEDs,[80] which is one of the few examples taking advantage of the above two properties simultaneously in graphene based LEDs. ZnO, CdS, and CdSe nanowires were employed to form face-to-face contact combined with graphene nanoribbons in the hybrid junction devices. The emitting wavelength of the as-fabricated LEDs can vary from ultraviolet (380 nm) to red (705 nm). Comparatively, it has been widely studied in solar cells and photodetectors to utilize the hetero-interface between graphene and semiconductors rather than the transparency, flexibility and conductivity of graphene. Thus, in the hybrid system between graphene and semiconductors, we will focus on the applications in solar cells and photodectors in the following parts.

4.1 Solar cells

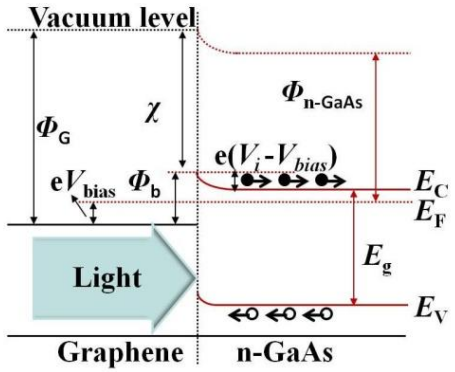

Fig. 10. The energy band diagram of graphene/n-GaAs Schottky junction under illumination. E_C, E_V, E_F, standing for the conduction band edge, valence band edge, and Fermi level of n-GaAs, respectively. E_g stands for the energy gap. Reproduced with permission from ref. 84. Copyright 2013 American Institute of Physics.

A solar cell device can convert light to electricity with a power conversion efficiency (PCE) which is equal to $V_{oc} \times J_{sc} \times FF / P_{inc}$, where V_{oc} is open-circuit voltage, J_{sc} is the short-circuit, FF is fill factor, and P_{inc} is the incident power. Currently, the most widely investigated solar cells are based on silicon with the efficiency of about 25% obtained from single p-n junction of crystalline Si, while GaAs-based solar cells show higher efficiency of more than 28%.[81] At early research stage in this field, graphene applied to solar cells has simply been used as an alternative transparent electrode to ITO due to its advantages, such as superior flexibility, higher transparency and better conductivity, no matter in inorganic silicon or organic polymer cells.[82,83] In fact, beyond the single role of transparent conductor, graphene can fulfil multiple functions in solar cells, such as photoactive layer, channel for charge transport, and catalyst. According to the band diagram of the forward-biased Schottky junction under illumination, taking graphene/n-GaAs as an example as schematically shown in Fig. 10,[84] the photo-generated carriers can be separated by the built-in field, and holes are diffused to the junction where they are swept to the graphene side. In principle, any semiconductor with electron affinity (χ) lower than the work function of graphene can create an M-S diode with Schottky-barrier height ($\Phi_b = \Phi_G - \chi$). As a consequence, a build-in potential ($eV_i = \Phi_G - \Phi_{n\text{-}GaAs}$) is generated in the semiconductor adjacent to the Schottky junction interface due to the different work function between them. Under the illumination, the photon-generated carriers can be separated and then transferred to the electrodes, yielding photovoltaic effects from such junction devices. Herein, based on the graphene/semiconductor structure, we focus on such Schottky junction solar cells, where CVD-grown graphene is generally

used when considering the scale effects of device.

4.1.1 Grpahene/Si junction solar cells.

Li et al reported graphene/Si Schottky junction solar cells by employing several layers of CVD-grown graphene sheets (GS). In their investigated junction solar cells, graphene was used as not only a transparent electrode for light illumination, but also an active layer for electron–hole separation and hole transport.[85,86] As illustrated in Fig. 11(a), graphene was coated onto a patterned n-Si/SiO_2 substrate with a small square window (contact area of 0.1 and 0.5 cm^2) and pre-deposited Au contacts around. Under air mass 1.5 (AM 1.5) illumination, light current density–voltage (*J*–*V*) data demonstrated down-shift curves with the V_{oc} of 0.42 ~ 0.48 V, J_{sc} of 4 ~ 6.5 mA cm^{-2}, and a fill factor of 45 ~ 56%, resulting in an overall solar energy PCE of 1.0 ~1.7%, as shown in Fig. 11(b). Additionally, the 0.1 cm^2 sized diode shows superior photovoltaic behaviours due to higher Schottky-barrier height and better rectifying characteristics compared to the 0.5 cm^2 sized one.

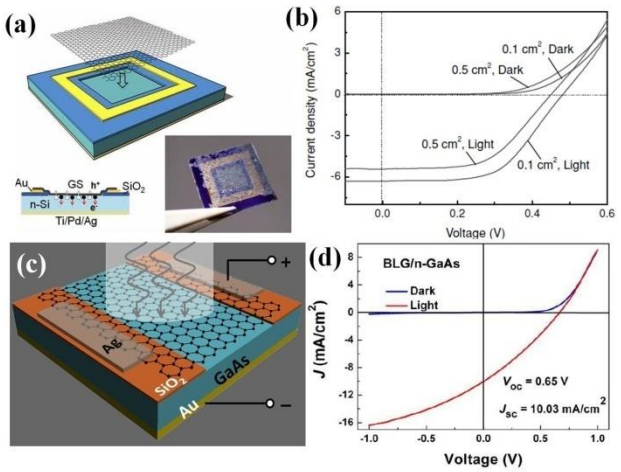

Fig. 11. Graphene/semiconductor junction solar cells. (a) Schematic of the graphene/Si Schottky junction solar cell device configuration. Bottom-left inset: cross-sectional view of such device, photogenerated holes (h^+) and electrons (e^-) are driven into the graphene and Si, respectively. Bottom-right inset: photograph of the Schottky junction device. (b) Dark and Light current density–voltage curves of the graphene/Si junction cells illuminated with simulated AM 1.5 Global light. Reproduced with permission from ref. 85. Copyright 2010 Wiley-VCH. (c) Schematic of graphene/GaAs Schottky junction solar cell with SiO_2 as an insulating layer. (d) The dark and light current density–voltage curves of the graphene/GaAs junction cells illuminated with simulated AM 1.5 Global light. Reproduced from ref. 84. Copyright 2013 American Institute of Physics.

4.1.2 Grpahene/GaAs junction solar cells.

In comparison with most commonly used Si, GaAs has the merits of higher saturated electron mobility and direct band gap, allowing GaAs-based devices to function at high frequencies, and be efficient in various optoelectronic devices in history. Previously, several types of heterostructures of perovskite oxide thin films and GaAs have been studied by our group.[87–93] Very recently, we combined CVD-grown graphene sheets with GaAs wafer. Single- and bi-layer graphene sheets were transferred onto n-type GaAs substrate with about 200-nm SiO_2 as insulating layer to form a graphene/GaAs Schottky barrier, as schematically shown in Fig. 11(c).[84] Among them, bilayer graphene/GaAs junction shows better photovoltaic behaviours with the V_{oc} of 0.65 V, J_{sc} of 10.03 mA/cm^2, yielding the PCE of 1.95 %. Such performance parameters of the device are comparable to above mentioned graphene/Si junction-based devices. While single-layer graphene-based device shows unexpectedly poor photovoltaic performance compared to the bilayer one, ascribing to its larger ideality factor, higher series resistance and lower Schottky-barrier height. By considering the high-performance of optoelectronic capabilities of radiation-resistant GaAs wafer, this work exhibits that the developed graphene/GaAs system may be an attractive system for future photovoltaic applications.

4.1.3 Graphene/nanowire or nanobelt junction solar cells.

The Schottky junction solar cells can be fabricated by combining graphene with other semiconductor nanostructures like CdS nanowire (NW) and CdSe nanobelt (NB)[94–96] Ye et al introduced 5 nm Au to graphene, serving as Schottky contact electrode to fabricate graphene-CdS single NW based junction solar cells.[96] In the combined Schottky electrode, the Au layer possessing high work-function benefits to build up a higher Schottky barrier with CdS NW, and the graphene helps to increase transparency and conductivity of the electrode. The fabricated Schottky junction solar cell shows the V_{oc} of 0.15 V and short-circuit current I_{sc} of 275 pA, producing a PCE of about1.65%. Such novel single CdS NW junction solar cells exhibit comparable photovoltaic performance to the wafer scale semiconductor ones, suggesting nanostructure semiconductors have the potential to function as an integrated power source in nano-optoelectronic systems. Additionally, a graphene-CdSe NB junction solar cell with the PCE of about 1.25% was prepared by the same research group.[95] In the reported junction device, graphene functions as the Schottky contact electrode, giving rise to the V_{oc} of 0.51 V and J_{sc} of 5.75 mA/cm^2.

4.1.4 Methods to improve the junction solar cells.

As above introduced, single-junction graphene-based photovoltaic devices have attracted much attention due to their simplifying fabrication process and potential widespread applications.[97–100] However, the conversion efficiency of pristine graphene-based cells is still not comparable to traditional Si or GaAs junction solar cells. To date, GaAs based multijunction devices are the most efficient solar cells, which ever reached a record as high as 37.9%.[101] As a result, many efforts have been put on to improve the performance of graphene-based Schottky junction solar cells. For example, chemical or substitutional doping to graphene layer can reduce graphene's sheet resistance or achieve p-type modification, and therefore increase the built-in potential. These would be beneficial to the reduction of the ohmic losses and the enhancement of the electron-hole pairs separation generated by absorbed photons. Different p-doping methods have been developed like chemically treatment with HNO_3[97] or $AuCl_3$ solution,[102] and thionyl chloride ($SOCl_2$) vapor,[103] direct incorporation of boron in CVD process.[104] Note that doping with

bis(trifluoromethanesulfonyl)-amide [$((CF_3SO_2)_2NH)$] (TFSA) can result in an about 3~5 times increase in PCE of the graphene/n-Si Schottky junction solar cell jumping from 1.9 to 8.6%.[105] In this experiment, spin-casting TFSA was performed on the top surface of the transferred graphene layer, as schematically shown in Fig. 12(a). As can be seen from Fig. 12(c), the J_{sc}, V_{oc}, and *FF* all increase for the graphene/n-Si solar cells upon doping with TFSA. The improved light harvesting in chemically doped graphene/n-Si Schottky junction solar devices has been attributed to the reduction of graphene's sheet resistance and an increase in the built-in potential. The method is considered as a practical, simple and scalable routine since device fabrication involves simple planar thin-film geometries, conventional graphene production techniques and uncomplicated spin-casting of organic layers. However, the stability of the organic overlayers has not been reported. In addition, the layer number of graphene should be carefully tuned to compromise the electrical and optical properties, including work function, sheet resistance and film transmittance.[100] Moreover, some antireflection techniques are effective ways to reduce the optical losses, such as the introduction of a pillar-array periodic patterned structure to Si.[106] Up to now, the largest PCE of graphene/Si junction solar cell was reported to be 14.5% through spin-coating the antireflection layer of TiO_2 onto graphene/Si,[107] as seen in Fig. 12(b) and (d). The results demonstrate a great promise in developing high-efficiency graphene/semiconductor solar cells. The detailed performance parameters of graphene-based Schottky junction solar cells with various methods to enhance the device performance are summarised in Table. 1

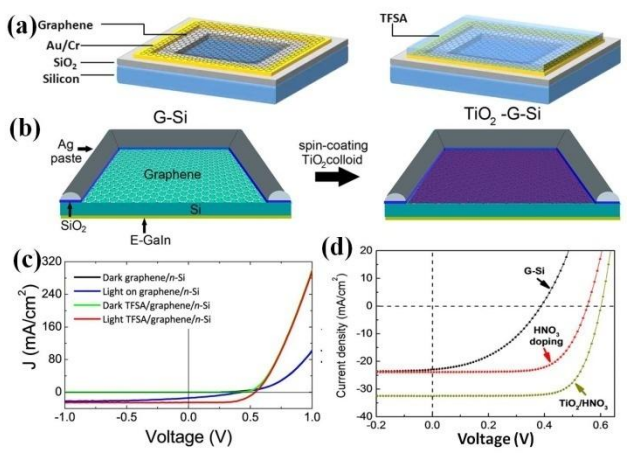

Fig. 12. The enhancement of performance for graphene/Si junction solar cells. (a) Schematic of Graphene/n-Si and TFSA doped graphene/n-Si Schottky solar cells. (b) Illustration of the spin-coating process in which a colloidal TiO_2 layer was applied to a graphene-Si junction cell as antireflection coating. (c) *J*–*V* characteristics of graphene/n-Si and doped-graphene/n-Si Schottky solar cells in dark and after illumination. Reproduced with permission from ref. 105. Copyright 2012 American Chemical Society. (d) *J*–*V* curves of an as-fabricated graphene-Si solar cell, after HNO_3 vapor doping, and after TiO_2 coating (combined with HNO_3 doping), respectively, under illumination. Reproduced with permission from ref. 107. Copyright 2013 American Chemical Society.

Table 1. Performance parameters of graphene-based Schottky junction solar cells combined with different semiconductors. Some methods are used to improve the performance of the solar cells.

Semi-conductor	Methods to improve performance	V_{oc} (V)	J_{sc} (mA/cm^2)	PCE	Ref.
Si	Pristine	0.48	6.5	1.65	85
GaAs	Pristine	0.65	10.03	1.95	84
GdSe NB	Pristine	0.51	5.75	1.25	95
CdS NW	Integrating 5-nm Au electrode	0.15	NA	1.65	96
Si NW	$SoCl_2$ doping	0.503	11.24	2.86	103
Si	Boron doping and HNO_3 modification	0.57	21	3.4	104
Si	Si-pillar-array and HNO_3 doping	0.515	22.7	7.72	106
Si	TFSA doping	0.54	25.3	8.6	105
Si	Multilayer graphene and HNO_3 doping	0.55	16.91	9.63	99
Si	TiO_2 coating and HNO_3 doping	0.62	32.5	14.5	107

4.2 Photodetectors

Graphene allows electron-hole pairs to be generated over a broad range of wavelength ranging from ultraviolet to terahertz due to the gapless band structure, and graphene exhibits ultrafast photo response thanks to its high carrier mobility. These properties enable graphene promising in photodetectors applications. Generally, there are two main types of photodetectors, namely photodiodes and photoconductors.[108] The former one relies on the junction built by two media with significant difference in their work functions. Under light, the electrons and holes generated by the incident photons move to an opposite direction, yielding a photocurrent corresponding to the light level. In photoconductors, the difference in conductance between in dark and light is examined to determine the light intensity. The first graphene-based photodetector was discovered by detecting the photocurrent arising from the band bending at the graphene/metal (Au or Ti) interface while locally gated by 300-nm SiO_2 from a back-gated graphene transistor grown on SiO_2/Si substrate.[109] Particularly, a strong photoresponse can be generated at the interfaces including single/bilayer graphene interfaces and the graphene p–n junctions.[110,111] At the interface, the photo-induced thermal effect

on graphene with different carrier density distribution can generate a detectable voltage or current across the graphene junction, which can be explained by the photothermoelectric effect.[112] Such photothermoelectric effect may be potentially exploited to make novel optoelectronic devices. Although the microscopic processes of photocurrent generation are still debated,[113–115] the complementary metal–oxide semiconductor (CMOS)-compatible graphene/silicon based photodetector devices are very appealing in many fields of potential applications. [116–119] In this section, optoelectronic devices integrated by graphene and Si semiconductor will be concentrated.

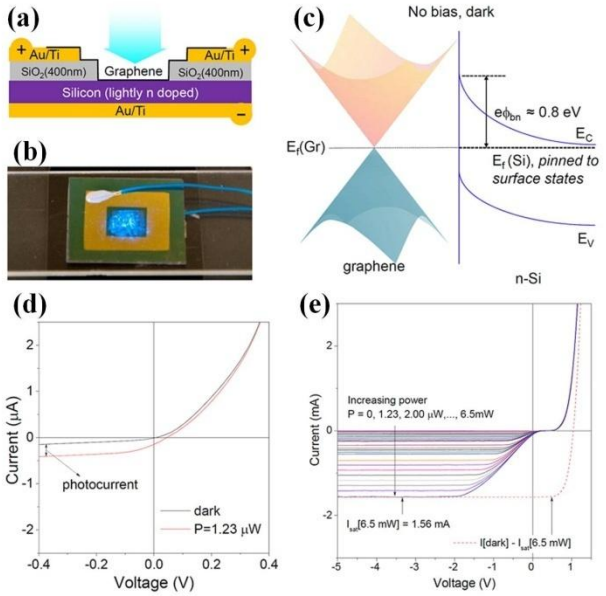

Fig. 13. Graphene/Si-heterojunction photodetector. (a) Schematic and (b) photograph of the device. (c) Thermal equilibrium energy band diagram of the heterojunction in darkness, with the band profile of n-Si pinned to the charge neutrality level of its own surface states. The dark Fermi level of graphene E_f(Gr) is also shown. (d) Current−voltage (*I*−*V*) curves of device A (area = 25 mm^2) under darkness and weak illumination (P = 1.23 μW, λ = 488 nm) showing a conventional photodiode-like behavior. (e) Deviation of the *I*−*V* curves from a conventional photodiode response as the incident light power is increased up to P = 6.5 mW. The expected ideal photodiode behavior at P = 6.5mW is plotted with a red dashed line. Reproduced with permission from ref. 120. Copyright 2013 American Chemical Society.

4.2.1 CVD-grown graphene/Si photodetector.

An et al reported CVD-grown monolayer graphene/Si heterojunction for ultrasensitive photodetection based on graphene/n-Si photodiode, as schematically shown in Fig. 13(a).[120] Fig. 13(b) presents a photograph of the device sample. In dark, as shown in Fig. 13(c), Schottky barrier with the height of 0.8 V was created due to the difference in Fermi levels of graphene and n-doped Si under thermal equilibrium. Under an illumination of light (λ = 488 nm) with low power, the rectifying current−voltage (*I*−*V*) curve exhibits a typical photodiode-like behaviours [Fig. 13(d)]. With increasing the power of incident light, a significant deviation of the *I*−*V* curves can be observed from the conventional photodiode-like response [Fig. 13(e)]. The *I*−*V* curve under higher incident power exhibits a strong suppression of photocurrents close to zero point and a sharp rise and rapid saturation of photocurrents at low reverse bias. This highly tunable photocurrent response up to 435 mA/W can be attributed to the unique electronic structure of graphene near its Fermi level. Under a low forward bias, the Fermi level is lowered from its "unbiased" position to the location closer to the quasi Fermi level for holes in Si, resulting in the reduction of the number of accessible states for the photo-excited carriers to inject into from Si. Therefore, the forward current is independent of the incident light power. Conversely, an applied reverse bias can lift the Fermi level to higher values, opening up a large number of accessible states for the holes to inject and allowing a complete collection of the injected holes. This work indicates that the graphene/Si system is attractive for excellent weak-signal photodetectors with high responsivity.

4.1.2 Mechanically exfoliated graphene/Si waveguide.

Direct and indirect transitions in mechanically exfoliated graphene/silicon heterostructure waveguides have been investigated for 1.55 and 2.75 μm mid-infrared (MIR) detection, respectively.[117] The detector was made by integrating graphene onto a silicon optical waveguide, as schematically shown in Fig. 14(a). The in-plane coupled waveguide is helpful to improve the graphene-light interaction, suppress the dark current and enhance the MIR absorbance. These photodetectors exhibit extremely large photoresponsivity in MIR band, resulting in a responsivity jumping up to as high as 0.13 A/W at a 1.5 V bias for 2.75 μm light at room temperature, as shown in Fig. 14 (b). Furthermore, such photodetectors can achieve an extremely large ON/OFF current ratio from the visible light to MIR range.

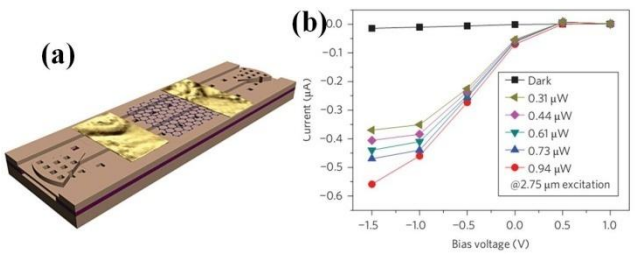

Fig. 14. Graphene/Si-heterostructure waveguide photodetector. (a) Schematic of the photodetector. (b) Infrared performance of photoresponse of the photodetector with the incident wavelength of 2.75 μm under different incident light powers. Reproduced with permission from ref. 117. Copyright 2013 Nature Publishing Group.

However, graphene-based devices restricted the photodetection to narrow bands, or sacrificed response speed. Because graphene is an inherently weak optical absorber (only ~2.3% absorption), novel concepts need to be developed to increase the spectral absorption and take full advantage of its unique optical properties. A number of recent works have focused on increasing the responsivity of the devices[121–124] and extending their operation range to longer wavelengths.[125,126] For example,

the integration of graphene and other nanostructures or microstructures, such as nanocavities,[127] microcavities[122] and plasmon resonators,[105] is capable of enhancing the photoresponsivity. Furchi et al proposed to integrate graphene with a Fabry-Pérot microcavity, the optical absorption was found to be 26-fold enhanced, reaching a responsivity of 21 mA/W.[122] Gan et al developed a metal-doped graphene junction coupled evanescently to the waveguide. A waveguide-integrated graphene photodetector was fabricated, which exhibits high responsivity exceeding 0.1 A/W, high speed exceeding and broad spectral bandwidth simultaneously.[127]

4.3 Heterostructure between graphene and 2D semiconductors

Graphene seems to be just the tip of the iceberg for 2D materials and the subsequent discovery of alternative 2D materials beyond graphene shows a big 2D family.[128] Indeed, the use of simple micro-mechanical cleavage technique proposed by Novoselov et al. has been expanded from graphene to other layered materials.[129] Among them, molybdenum disulfide (MoS_2), is a typical example with exotic properties. The band gap of MoS_2 shifts from the indirect gap of 1.29 eV to direct gap of over 1.90 eV when decreasing the thickness of MoS_2 from bulk to single layer.[130]

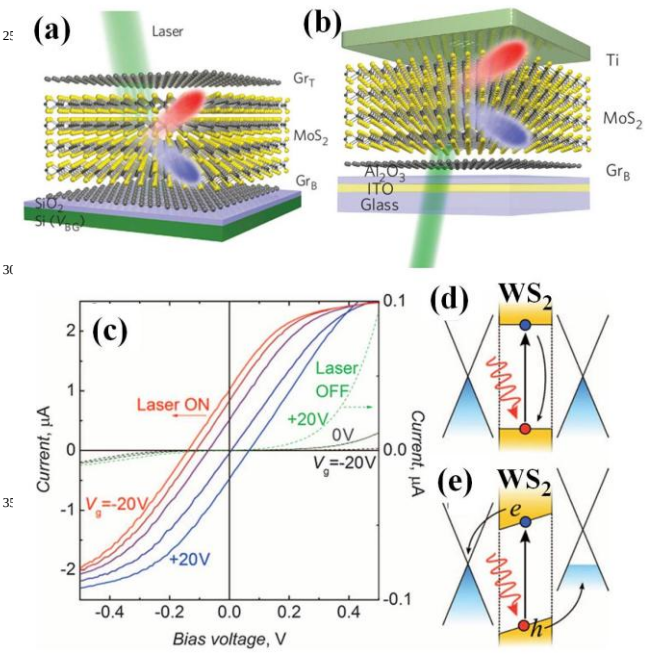

Fig. 15. The hybrid structure between graphene and 2D semiconductors. The schematic of vertical heterostructure of (a) graphene-MoS_2-graphene with SiO_2 as bottom gate and (b) graphene-MoS_2-metal with Al_2O_3 as top gate. Reproduced with permission from ref. 144. Copyright 2013 Nature Publishing Group. (c) The gate-dependent *I*–*V* curves of graphene-WS_2-graphene heterostructure with SiO_2 as bottom gate under dark and laser illumination (2.54 eV, 10 μW). The gate voltage changes from −20 V to 20 V. Schematic band diagram for graphene-WS_2-graphene heterostructure with (d) and without (e) a built-in electric field to separate the generated electron-hole pairs. Reproduced with permission from ref. 145. Copyright 2013 American Association for the Advancement of Science.

Following a roadmap of graphene, layered MoS_2 has been integrated with versatile functional materials. Exfoliated MoS_2 was ever combined with traditional SiO_2 to form FETs, and also incorporated with HfO_2 as a top gate to fabricate dual gate FETs.[131] Such transistor exhibits a high mobility of 200 cm^2/Vs and a high ON/OFF ratio of 10^8. Furthermore, Lee et al demonstrated MoS_2-based non-volatile memory by using ferroelectric polymer of PVDF as a top gate.[132] Hui et al reported strain engineering in CVD-grown MoS_2 sheets by utilizing piezoelectric effect of PMN-PT single crystal.[133] Because monolayer MoS_2 is a direct-bandgap semiconductor, it should be more suitable for applications in optoelectronic devices where a high absorption coefficient and efficient electron-hole pair generation under photo-excitation. The basic application of MoS_2 would be as a semiconducting channel in phototransistors, where light would be directly converted into current. Accordingly, the first monolayer MoS_2-based phototransistor exhibits a photoresponsivity of 7.5 mA/W, which is comparable to graphene-based devices.[134] Then, such monolayer MoS_2-based phototransistors have been optimised to obtain a photoresponsivity of 880 A/W at a wavelength of 561 nm due to its improved mobility, as well as the contact quality and positioning technique.[135] With recent developments in large-scale production techniques such as CVD-like growth,[136,137] layered MoS_2 shows some inspiring characteristics for applications in integrated devices because of the presence of bandgap. Additionally, as a semiconductor, MoS_2 has been integrated with metal (Pd and Au) to form a Schottky junction with photovoltaic behaviours.[138] Beside MoS_2, hexagonal GaS and GaSe have layered structures with each layer consisting of S–Ga–Ga–S and Se–Ga–Ga–Se sheets, and indirect bandgaps of 3.05 eV and 2.1 eV, respectively.[139] Both of the new 2D materials have been employed in Si integrated devices, such as FETs and photodetectors.[140–143]

On the other hand, it has been proven feasible to integrate graphene of semi-metal and other 2D layered materials, such as semiconductors of MoS_2[144] and tungsten disulfide (WS_2)[145,146] or insulator of thexagonal boron nitride (hBN),[147–149] to obtain novel functions of highly efficient photoresponse, tunnelling transistors, Coulomb drag and fractional quantum Hall effect. The light-matter interaction could become stronger by making a heterostructure to become so thin that it has negligible thickness relative to the wavelength of light. For example, graphene/MoS_2 and graphene/WS_2 vertical heterostructure-based photodetectors may exhibiti a controllable photocurrent which can be tuned by an external electric field. Yu et al reported vertically stacked graphene-MoS_2-graphene and graphene-MoS_2-metal junctions for highly efficient photocarrier generation, separation and transport.[144] Fig. 15(a) shows the schematic of single-gated graphene-MoS_2-graphene heterostructure. The underlying SiO_2 functions as a back gate to modulate charge transport across the stacked structure. The barrier height of Schottky junction between graphene and MoS_2 can be tuned by the bottom gate voltage. Under the illumination by a focused laser with a

wavelength of 512 nm, the device shows photovoltaic behaviours. Additionally, the top layer of graphene also can be replaced by Ti to achieve an asymmetrical vertical heterostructure of graphene-MoS_2-metal with bottom Al_2O_3 gate, as shown in Fig. 15(b). With a graphene-MoS_2 Schottky contact and a nearly ohmic MoS_2-Ti contact, the asymmetric device could allow for further enhancement of the photocurrent. Britnell et al. combined highly conductive graphene and optically active 2D TMDC of WS_2 into a heterostructure that photoexcites electron-hole pairs within a band-gap material.[145] A graphene-WS_2-graphene heterostructure with SiO_2 as a back gate, showing a gate dependent photoresponse, as illustrated in Fig. 15(c). The bandgap of WS_2 is shifted from indirect bandgap (1.4 eV) in bulk semiconductor into direct bandgap (2.1 eV) in monolayer state. In dark, the heterojunction shows strong non-linear behaviours, while the *I*−*V* curves become nearly linear around zero bias under illumination and show strong dependence on the gate voltage. The operation principle of the device is that the photon-generated electrons/holes in WS_2 can be separated and show preferred diffusion direction in the presence of a built-in electric field induced by the difference in the initial doping between the graphene sheets or by gating. The schematic of band diagram with and without the built-in electric field is shown in Fig. 15 (d) and (e), respectively. Based on such heterostructure, large photon absorption and photocurrent have been achieved to reach an extremely large external quantum efficiency of 30% and photoresponsivity above 0.1 A/W by adding layers of hexagonal BN and depositing gold nanoparticles. Such new-developed heterostructures between 2D materials not only construct atomically thin film devices, but also possess novel functions and show potential applications for future nanophotonic devices.

Based on the above 2D heterostructure, it was proposed that a combination of two 2D materials could enable the fabrication of photonic devices based on extreme interactions between electrons and light.[150] As a result, the hybrid devices combined two 2D materials are better than single one in the aspects of electric and photonic properties. Indeed, new nanosystems can be created by coupling graphene to both 2D and 1-dimentional (1D) materials, such as carbon nanotubes (CNTs). For instance, synergistic assembly of 2D graphene and 1D CNTs may offer an opportunity to obtain multifunctional, ultra-lightweight and super-elastic carbon aerogels,[151,152] suggesting the excellent and novel properties of the combined nanomaterials. As a result, future nanoelectronic and nanophotonic devices can benefit from the combination of two or even more 2D materials to fabricate 2D heterostructure, which is an appealing choice for improving the properties of nanomaterials and enhancing the performances of nanoscale integrated hybrid devices.

Conclusions and perspectives

In this article, various hybrid systems consisting of graphene and functional materials ranging from ferroelectrics to semiconductors, have been introduced in the aspects of fabrication process, working principle, and potential applications. Based on graphene/ferroelectric hybrid systems, a wide range of electronic devices have been exhibited in the forms of non-volatile memories, transparent flexible electrodes, strain engineering in graphene sheets, as well as the pyroelectric transistors. By integrating graphene with ferroelectric PZT, PMN-PT, or organic PVDF, a varity of novel electronic devices have shown attractive potential for widespread application in future electronic and optical devices. For graphene/semiconductor hybrid systems, we focus on reviewing the status of Schottky junction built by graphene and some semiconductors, including traditional semiconductors (Si and GaAs) and newly-developed 2D layered MoS_2 and WS_2. Based on the diode junction, graphene-based solar cells and photodetectors can be achieved. Subsequently, many efforts have been paid to improve the device performances of graphene-based solar cells and photodetectors. It is shown that some effective techniques, such as modification by chemical doping and/or adding antireflection layer to graphene sheets, should be feasible ways to enhance the performance of graphene-based single junction solar cells. For graphene-based photodetectors, the phototransistors gated by SiO_2 or/and other dielectric materials have drawn much attention due to the matured fabrication process based on graphene FETs. Lastly, vertical packed nanoscale devices integrated with graphene and other 2D layered semiconductors not only realise atomically thin film devices, but also possess novel functions. It is hoped that hybrid systems of graphene-functional materials will become important components for widespread potential applications.

The functional materials compatible with graphene sheets have shown a wide range of spectrum, from initial gate insulator SiO_2, to a variety of functional oxides, including specific ferroelectrics, then to various conventional semiconductors, and now to atomically layered 2D TMDCs. Some newly discovered 2D materials are currently following the roadmap of graphene, which may offer great potential of being combined with bulk functional materials. By considering successful isolation of various 2D materials and advance in characterization techniques, it is worthwhile to note that a combination of two or even more types of 2D materials together in vertical stacks would be an important subject. This concept has created a new paradigm in materials science, namely heterostructures based on atomically thin films with novel functions. More importantly, some concepted devices have been proven feasible for future nanoelectronic and nanophotonic applications in the areas of ultrathin and flexible devices. The combination of different classes of 2D materials will open a door for the next generation of nanoelectronic and nanophotonic devices, such as nanoscale solar cells, light-emitting diodes, lasers, and photodetectors.

Notes

[a]*Department of Applied Physics, The Hong Kong Polytechnic University, Hung Hom, Kowloon, Hong Kong. Tel: (852)27664098; E-mail: jh.hao@polyu.edu.hk*
[b]*The Hong Kong Polytechnic University Shenzhen Research Institute, Shenzhen 518057, China.*

Acknowledgement

The authors gratefully acknowledge financial support from the

National Natural Science Foundation of China (No. 51272218).

References.

1. K. S. Novoselov, A. K. Geim, S. V. Morozov, D. Jiang, Y. Zhang, S. V. Dubonos, I. V. Grigorieva, and A. A. Firsov, *Science*, 2004, **306**, 666–669.
2. A. Bianco, H.-M. Cheng, T. Enoki, Y. Gogotsi, R. H. Hurt, N. Koratkar, T. Kyotani, M. Monthioux, C. R. Park, J. M. D. Tascon, and J. Zhang, *Carbon*, 2013, **65**, 1–6.
3. A. K. Geim and K. S. Novoselov, *Nat. Mater.*, 2007, **6**, 183–191.
4. A. K. Geim, *Science*, 2009, **324**, 1530–1534.
5. S. Morozov, K. Novoselov, M. Katsnelson, F. Schedin, D. Elias, J. Jaszczak, and A. K. Geim, *Phys. Rev. Lett.*, 2008, **100**, 016602.
6. J. Chen, C. Jang, S. Adam, M. S. Fuhrer, E. D. Williams, and M. Ishigami, 2008, **3**, 377–381.
7. J.-H. Chen, C. Jang, S. Xiao, M. Ishigami, and M. S. Fuhrer, *Nat. Nanotechnol.*, 2008, **3**, 206–209.
8. V. Berry, *Carbon*, 2013, **62**, 1–10.
9. Y. Zhao, Y. Xie, Y. Y. Hui, L. Tang, W. Jie, Y. Jiang, L. Xu, S. P. Lau, and Y. Chai, *J. Mater. Chem. C*, 2013, **1**, 4956–4961.
10. A. A. Balandin, S. Ghosh, W. Bao, I. Calizo, D. Teweldebrhan, F. Miao, and C. N. Lau, *Nano Lett.*, 2008, **8**, 902–907.
11. X. Li, Y. Zhu, W. Cai, M. Borysiak, and B. Han, *Nano Lett.*, 2009, **9**, 4359–4363.
12. C. Lee, X. Wei, J. W. Kysar, and J. Hone, *Science*, 2008, **321**, 385–388.
13. Q. Bao and K. P. Loh, *ACS Nano*, 2012, **6**, 3677–3694.
14. Y. Zhu, S. Murali, W. Cai, X. Li, J. W. Suk, J. R. Potts, and R. S. Ruoff, *Adv. Mater.*, 2010, **22**, 3906–3924.
15. K. S. Novoselov, Z. Jiang, Y. Zhang, S. V. Morozov, H. L. Stormer, U. Zeitler, J. C. Maan, G. S. Boebinger, P. Kim, and A. K. Geim, *Science*, 2007, **315**, 1379.
16. F. Schwierz, *Nat. Nanotechnol.*, 2010, **5**, 487–496.
17. S. X. Wang, J. H. Hao, Z. P. Wu, D. Y. Wang, Y. Zhuo, and X. Z. Zhao, *Appl. Phy. Lett.*, 2007, **91**, 252908.
18. J. Hao, W. Si, X. X. Xi, R. Guo, A. S. Bhalla, and L. E. Cross, *Appl. Phy. Lett.*, 2000, **76**, 3100–3102.
19. J. S. Wu, C. L. Jia, K. Urban, J. H. Hao, and X. X. Xi, *J. Mater. Res.*, 2001, **16**, 3443–3450.
20. C. Ang, L.E. Cross, Z. Yu, R. Guo, A. S. Bhalla, J. H. Hao, *Appl. Phy. Lett.*, 2001, **78**, 2754–2756.
21. Y. Zhang and J. Hao, *J. Appl. Phys.* 2013, **113**, 184112.
22. Y. Zhang and J. Hao, *J. Mater. Chem. C*, 2013, **1**, 5607–5618.
23. J. Hao, Y. Zhang, and X. Wei, *Angew. Chem. Int. Ed.*, 2011, **50**, 6876–6880.
24. Y. Zhang, J. Hao, C. L. Mak, and X. Wei, *Optics Express*, 2011, **19**, 1824–1829.
25. T. Wu, A. Bur, K. Wong, P. Zhao, and C. S. Lynch, *Appl. Phys. Lett.*, 2011, **98**, 262504.
26. A. Kingon, *Nature*, 1999, **401**, 658–659.
27. G. Ni, Y. Zheng, S. Bae, C. Tan, O. Kahya, J. Wu, B. H. Hong, K. Yao, and B. Özyilmaz, *ACS Nano*, 2012, **6**, 3935–3942.
28. X. Hong, A. Posadas, K. Zou, C. Ahn, and J. Zhu, *Phys. Rev. Lett.*, 2009, **102**, 136808.
29. S.-H. Bae, O. Kahya, B. K. Sharma, J. Kwon, H. J. Cho, B. Ozyilmaz, and J.-H. Ahn, *ACS Nano*, 2013, **7**, 3130–3138.
30. H. Yang, J. Heo, S. Park, H. J. Song, D. H. Seo, K.-E. Byun, P. Kim, I. Yoo, H.-J. Chung, and K. Kim, *Science*, 2012, **336**, 1140–1143.
31. S. Tongay, T. Schumann, X. Miao, B. R. Appleton, and A. F. Hebard, *Carbon*, 2011, **49**, 2033–2038.
32. S. Tongay, T. Schumann, and A. F. Hebard, *Appl. Phys. Lett.*, 2009, **95**, 222103.
33. S. Tongay, M. Lemaitre, T. Schumann, K. Berke, B. R. Appleton, B. Gila, and A. F. Hebard, *Appl. Phys. Lett.*, 2011, **99**, 102102.
34. C.-C. Chen, C.-C. Chang, Z. Li, A. F. J. Levi, and S. B. Cronin, *Appl. Phys. Lett.*, 2012, **101**, 223113.
35. X. Wu, M. Sprinkle, X. Li, F. Ming, C. Berger, and W. de Heer, *Phys. Rev. Lett.*, 2008, **101**, 026801.
36. Y. Ye and L. Dai, *J. Mater. Chem.*, 2012, **22**, 24224–24229.
37. K. S. Kim, Y. Zhao, H. Jang, S. Y. Lee, J. M. Kim, K. S. Kim, J.-H. Ahn, P. Kim, J.-Y. Choi, and B. H. Hong, *Nature*, 2009, **457**, 706–710.
38. X. Li, W. Cai, J. An, S. Kim, J. Nah, D. Yang, R. Piner, A. Velamakanni, I. Jung, E. Tutuc, S. K. Banerjee, L. Colombo, and R. S. Ruoff, *Science*, 2009, **324**, 1312–1314.
39. S. Bae, H. Kim, Y. Lee, X. Xu, J.-S. Park, Y. Zheng, J. Balakrishnan, T. Lei, H. R. Kim, Y. I. Song, Y.-J. Kim, K. S. Kim, B. Ozyilmaz, J.-H. Ahn, B. H. Hong, and S. Iijima, *Nat. Nanotechnol.*, 2010, **5**, 574–578.
40. L. Gao, W. Ren, H. Xu, L. Jin, Z. Wang, T. Ma, L.-P. Ma, Z. Zhang, Q. Fu, L.-M. Peng, X. Bao, and H.-M. Cheng, *Nat. Commun.*, 2012, **3**, 699.
41. K. V. Emtsev, A. Bostwick, K. Horn, J. Jobst, G. L. Kellogg, L. Ley, J. L. McChesney, T. Ohta, S. A. Reshanov, J. Röhrl, E. Rotenberg, A. K. Schmid, D. Waldmann, H. B. Weber, and T. Seyller, *Nat. Mater.*, 2009, **8**, 203–207.
42. P. W. Sutter, J.-I. Flege, and E. A. Sutter, *Nat. Mater.*, 2008, **7**, 406–411.
43. S. Stankovich, D. A. Dikin, R. D. Piner, K. A. Kohlhaas, A. Kleinhammes, Y. Jia, Y. Wu, S. T. Nguyen, and R. S. Ruoff, *Carbon*, 2007, **45**, 1558–1565.
44. H. Wang, J. T. Robinson, X. Li, and H. Dai, *J. Am. Chem. Soc.*, 2009, **131**, 9910–9911.
45. X. Li, G. Zhang, X. Bai, X. Sun, X. Wang, E. Wang, and H. Dai, *Nat. Nanotechnol.*, 2008, **3**, 538–542.
46. Y. Zheng, G.-X. Ni, C.-T. Toh, M.-G. Zeng, S.-T. Chen, K. Yao, and B. Özyilmaz, *Appl. Phys. Lett.*, 2009, **94**, 163505.
47. X. Hong, J. Hoffman, A. Posadas, K. Zou, C. H. Ahn, and J. Zhu, *Appl. Phys. Lett.*, 2010, **97**, 033114.
48. Y. Zheng, G.-X. Ni, C.-T. Toh, C.-Y. Tan, K. Yao, and B. Özyilmaz, *Phys. Rev. Lett.*, 2010, **105**, 166602.
49. Y. Zheng, G.-X. Ni, S. Bae, C.-X. Cong, O. Kahya, C.-T. Toh, H. R. Kim, D. Im, T. Yu, J. H. Ahn, B. H. Hong, and B. Özyilmaz, *Europhys. Lett.*, 2011, **93**, 17002.
50. S. Raghavan, I. Stolichnov, N. Setter, J. Heron, M. Tosun, and A. Kis, *Appl. Phys. Lett.*, 2012, **100**, 023507.
51. E. B. Song, B. Lian, S. M. Kim, S. Lee, T. Chung, M. Wang, C. Zeng, G. Xu, K. Wong, Y. Zhou, H. I. Rasool, D. H. Seo, H. Chung, J. Heo, S. Seo, and K. L. Wang, *Appl. Phys. Lett.*, 2011, **99**, 042109.
52. C. Baeumer, S. Rogers, R. Xu, L. Martin, and M. Shim, *Nano Lett.*, 2013, **13**, 1693–1698.
53. W. Jie, Y. Y. Hui, N. Y. Chan, Y. Zhang, S. P. Lau, and J. Hao, *J. Phys. Chem. C*, 2013, **117**, 13747–13752.
54. H. Romero, N. Shen, and P. Joshi, *ACS Nano*, 2008, **2**, 2037–2044.
55. K. S. Novoselov, A. K. Geim, S. V. Morozov, D. Jiang, Y. Zhang, S. V. Dubonos, I. V. Grigorieva, and A. A. Firsov, *Science*, 2004, **306**, 666–669.
56. J. Baltazar, H. Sojoudi, S. A. Paniagua, J. Kowalik, S. R. Marder, L. M. Tolbert, S. Graham, and C. L. Henderson, *J. Phys. Chem. C*, 2012, **116**, 19095–19103.
57. H. Hwang, P. Joo, M. Kang, G. Ahn, J. Han, B.-S. Kim, and H. H. Cho, *ACS Nano*, 2012, **6**, 2432–2440.
58. G. Giovannetti, P. Khomyakov, G. Brocks, V. Karpan, J. van den Brink, and P. Kelly, *Phys. Rev. Lett.*, 2008, **101**, 026803.
59. J. S. Lee, S. Ryu, K. Yoo, I. S. Choi, W. S. Yun, and J. Kim, *J. Phys. Chem. C*, 2007, **111**, 12504–12507.
60. Z. Liu, J. Li, Z.-H. Sun, G. Tai, S.-P. Lau, and F. Yan, *ACS Nano*, 2012, **6**, 810–818.
61. A. Kasry, M. A. Kuroda, G. J. Martyna, G. S. Tulevski, and A. A. Bol, *ACS Nano*, 2010, **4**, 3839–3844.
62. F. Gu, H. Shin, C. Biswas, G. H. Han, E. S. Kim, and S. J. Chae, *ACS Nano*, 2010, **4**, 4595–4600.
63. C. Yan, K.-S. Kim, S.-K. Lee, S.-H. Bae, B. H. Hong, J.-H. Kim, H.-J. Lee, and J.-H. Ahn, *ACS Nano*, 2012, **6**, 2096–2103.
64. B. Chandra, A. Afzali, N. Khare, M. M. El-Ashry, and G. S. Tulevski, *Chem. Mater.*, 2010, **22**, 5179–5183.
65. X.-W. Fu, Z.-M. Liao, J.-X. Zhou, Y.-B. Zhou, H.-C. Wu, R. Zhang, G. Jing, J. Xu, X. Wu, W. Guo, and D. Yu, *Appl. Phys. Lett.*, 2011, **99**, 213107.

66. Y. Zhang, G. Gao, H. L. W. Chan, J. Dai, Y. Wang, and J. Hao, *Adv. Mater.*, 2012, **24**, 1729–1735.
67. J. Zabel, R. R. Nair, A. Ott, T. Georgiou, A. K. Geim, K. S. Novoselov, and C. Casiraghi, *Nano Lett.*, 2012, **12**, 617–621.
68. J.-U. Lee, D. Yoon, and H. Cheong, *Nano Lett.*, 2012, **12**, 4444–4448.
69. O. Frank, G. Tsoukleri, J. Parthenios, K. Papagelis, I. Riaz, R. Jalil, K. S. Novoselov, and C. Galiotis, *ACS Nano*, 2010, **4**, 3131–3138.
70. Z. H. Ni, T. Yu, Y. H. Lu, Y. Y. Wang, Y. P. Feng, and Z. X. Shen, *ACS Nano*, 2008, **2**, 2301–2305.
71. Y.-H. Lee and Y.-J. Kim, *Appl. Phys. Lett.*, 2012, **101**, 083102.
72. T. Mohiuddin, A. Lombardo, R. Nair, A. Bonetti, G. Savini, R. Jalil, N. Bonini, D. Basko, C. Galiotis, N. Marzari, K. Novoselov, A. Geim, and A. Ferrari, *Phys. Rev. B*, 2009, **79**, 205433.
73. T. Yu, Z. Ni, C. Du, Y. You, Y. Wang, and Z. Shen, *J. Phys. Chem. C*, 2008, **112**, 12602–12605.
74. F. Ding, H. Ji, Y. Chen, A. Herklotz, K. Dörr, Y. Mei, A. Rastelli, and O. G. Schmidt, *Nano Lett.*, 2010, **10**, 3453–3458.
75. W. Jie, Y. Yu Hui, Y. Zhang, S. Ping Lau, and J. Hao, *Appl. Phys. Lett.*, 2013, **102**, 223112.
76. C.-Y. Hsieh, Y.-T. Chen, W.-J. Tan, Y.-F. Chen, W. Y. Shih, and W.-H. Shih, *Appl. Phys. Lett.*, 2012, **100**, 113507.
77. S. Pang, Y. Hernandez, X. Feng, and K. Müllen, *Adv. Mater.*, 2011, **23**, 2779–2795.
78. F. Bonaccorso, Z. Sun, T. Hasan, and A. C. Ferrari, *Nat. Photon.*, 2010, **4**, 611–622.
79. R.-H. Kim, M.-H. Bae, D. G. Kim, H. Cheng, B. H. Kim, D.-H. Kim, M. Li, J. Wu, F. Du, H.-S. Kim, S. Kim, D. Estrada, S. W. Hong, Y. Huang, E. Pop, and J. A. Rogers, *Nano Lett.*, 2011, **11**, 3881–3886.
80. Y. Ye, L. Gan, L. Dai, H. Meng, F. Wei, Y. Dai, Z. Shi, B. Yu, X. Guo, and G. Qin, *J. Mater. Chem.*, 2011, **21**, 11760–11763.
81. M. A. Green, K. Emery, Y. Hishikawa, W. Warta, and E. D. Dunlop, *Prog. Photovolt: Res. Appl.*, 2012, **20**, 12–20.
82. X. Wang, L. Zhi, and K. Mu, *Nano Lett.*, 2008, **8**, 323–327.
83. Z. Yin, S. Wu, X. Zhou, X. Huang, Q. Zhang, F. Boey, and H. Zhang, *Small*, 2010, **6**, 307–312.
84. W. Jie, F. Zheng, and J. Hao, *Appl. Phys. Lett.*, 2013, **103**, 233111.
85. X. Li, H. Zhu, K. Wang, A. Cao, J. Wei, C. Li, Y. Jia, Z. Li, X. Li, and D. Wu, *Adv. Mater.*, 2010, **22**, 2743–2748.
86. R. Won, *Nat. Photon.*, 2010, **4**, 411.
87. X. H. Wei, W. Huang, Z. B. Yang, and J. H. Hao, *Scripta Mater.*, 2011, **65**, 323–326.
88. W. Huang, Z. P. Wu, and J. H. Hao, *Appl. Phys. Lett.*, 2009, **94**, 032905.
89. Z. Yang, W. Huang, and J. Hao, *Appl. Phys. Lett.*, 2013, **103**, 031919.
90. G. Y. Gao, Z. B. Yang, W. Huang, H. Z. Zeng, Y. Wang, H. L. W. Chan, W. B. Wu, and J. H. Hao, *J. Appl. Phys.*, 2013, **114**, 094106.
91. Z. Yang and J. Hao, *J. Appl. Phys.*, 2012,**112**, 054110.
92. W. Huang, J. Y. Dai, J. H. Hao, *Appl. Phys. Lett.*, 2010, **97**, 162905.
93. Z. P. Wu, W. Huang, K. H. Wong, J. H. Hao, *J. Appl. Phys.*, 2008, **104**, 054103.
94. W. Jin, Y. Ye, L. Gan, B. Yu, P. Wu, Y. Dai, H. Meng, X. Guo, and L. Dai, *J. Mater. Chem.*, 2012, **22**, 2863–2687.
95. Y. Ye, L. Gan, L. Dai, Y. Dai, X. Guo, H. Meng, B. Yu, Z. Shi, K. Shang, and G. Qin, *Nanoscale*, 2011, **3**, 1477–1481.
96. Y. Ye, Y. Dai, L. Dai, Z. Shi, N. Liu, F. Wang, L. Fu, R. Peng, X. Wen, Z. Chen, Z. Liu, and G. Qin, *ACS Appl. Mater. Interfaces*, 2010, **2**, 3406–3410.
97. T. Feng, D. Xie, Y. Lin, Y. Zang, T. Ren, R. Song, H. Zhao, H. Tian, X. Li, H. Zhu, and L. Liu, *Appl. Phys. Lett.*, 2011, **99**, 233505.
98. Z. Li, H. Zhu, D. Xie, K. Wang, A. Cao, J. Wei, X. Li, L. Fan, and D. Wu, *Chem. Commun.*, 2011, **47**, 3520–3522.
99. X. Li, D. Xie, H. Park, M. Zhu, T. H. Zeng, K. Wang, J. Wei, D. Wu, J. Kong, and H. Zhu, *Nanoscale*, 2013, **5**, 1945–1948.
100. X. Li, D. Xie, H. Park, T. H. Zeng, K. Wang, J. Wei, M. Zhong, D. Wu, J. Kong, and H. Zhu, *Adv. Energy Mater.*, 2013, **3**, 1029–1034.
101. M. A. Green, K. Emery, Y. Hishikawa, W. Warta, and E. D. Dunlop, *Prog. Photovolt: Res. Appl.*, 2013, 827–837.
102. Y. Shi, K. K. Kim, A. Reina, M. Hofmann, L.-J. Li, and J. Kong, *ACS Nano*, 2010, **4**, 2689–2694.
103. G. Fan, H. Zhu, K. Wang, J. Wei, X. Li, Q. Shu, N. Guo, and D. Wu, *ACS Appl. Mater. Interfaces*, 2011, **3**, 721–725.
104. X. Li, L. Fan, Z. Li, K. Wang, M. Zhong, J. Wei, D. Wu, and H. Zhu, *Adv. Energy Mater.*, 2012, **2**, 425–429.
105. X. Miao, S. Tongay, M. K. Petterson, K. Berke, A. G. Rinzler, B. R. Appleton, and A. F. Hebard, *Nano Lett.*, 2012, **12**, 2745–2750.
106. Y. Lin, X. Li, D. Xie, T. Feng, Y. Chen, R. Song, H. Tian, T. Ren, M. Zhong, K. Wang, and H. Zhu, *Energy Environ. Sci.*, 2013, **6**, 108–115.
107. E. Shi, H. Li, L. Yang, L. Zhang, Z. Li, P. Li, Y. Shang, S. Wu, X. Li, J. Wei, K. Wang, H. Zhu, D. Wu, Y. Fang, and A. Cao, *Nano Lett.*, 2013, **13**, 1776–1781.
108. G. Konstantatos and E. H. Sargent, *Nat. Nanotechnol.*, 2010, **5**, 391–400.
109. E. J. H. Lee, K. Balasubramanian, R. T. Weitz, M. Burghard, and K. Kern, *Nat. Nanotechnol.*, 2008, **3**, 486–490.
110. M. C. Lemme, F. H. L. Koppens, A. L. Falk, M. S. Rudner, H. Park, L. S. Levitov, and C. M. Marcus, *Nano Lett.*, 2011, **11**, 4134–4137.
111. X. Xu, N. M. Gabor, J. S. Alden, A. M. van der Zande, and P. L. McEuen, *Nano Lett.*, 2010, **10**, 562–566.
112. D. Basko, *Science*, 2011, **334**, 610–611.
113. J. C. W. Song, M. S. Rudner, C. M. Marcus, and L. S. Levitov, *Nano Lett.*, 2011, **11**, 4688–4692.
114. M. Freitag, T. Low, F. Xia, and P. Avouris, *Nat. Photon.*, 2012, **7**, 53–59.
115. N. M. Gabor, J. C. W. Song, Q. Ma, N. L. Nair, T. Taychatanapat, K. Watanabe, T. Taniguchi, L. S. Levitov, and P. Jarillo-Herrero, *Science*, 2011, **334**, 648–652.
116. A. Pospischil, M. Humer, M. M. Furchi, D. Bachmann, R. Guider, T. Fromherz, and T. Mueller, *Nat. Photon.*, 2013, **7**, 892–896.
117. X. Wang, Z. Cheng, K. Xu, H. K. Tsang, and J.-B. Xu, *Nat. Photon.*, 2013, **7**, 888–891.
118. X. Gan, R.-J. Shiue, Y. Gao, I. Meric, T. F. Heinz, K. Shepard, J. Hone, S. Assefa, and D. Englund, *Nat. Photon.*, 2013, **7**, 883–887.
119. K. Kim, J.-Y. Choi, T. Kim, S.-H. Cho, and H.-J. Chung, *Nature*, 2011, **479**, 338–344.
120. X. An, F. Liu, Y. J. Jung, and S. Kar, *Nano Lett.*, 2013, **13**, 909–916.
121. G. Konstantatos, M. Badioli, L. Gaudreau, J. Osmond, M. Bernechea, F. P. Garcia de Arquer, F. Gatti, and F. H. L. Koppens, *Nat. Nanotechnol.*, 2012, **7**, 363–368.
122. M. Furchi, A. Urich, A. Pospischil, G. Lilley, K. Unterrainer, H. Detz, P. Klang, A. M. Andrews, W. Schrenk, G. Strasser, and T. Mueller, *Nano Lett.*, 2012, **12**, 2773–2777.
123. Y. Liu, R. Cheng, L. Liao, H. Zhou, J. Bai, G. Liu, L. Liu, Y. Huang, and X. Duan, *Nat. Commun.*, 2011, **2**, 579.
124. T. J. Echtermeyer, L. Britnell, P. K. Jasnos, A. Lombardo, R. V. Gorbachev, A. N. Grigorenko, A. K. Geim, A. C. Ferrari, and K. S. Novoselov, *Nat. Commun.*, 2011, **2**, 458.
125. L. Vicarelli, M. S. Vitiello, D. Coquillat, A. Lombardo, A. C. Ferrari, W. Knap, M. Polini, V. Pellegrini, and A. Tredicucci, *Nat. Mater.*, 2012, **11**, 865–871.
126. J. Yan, M.-H. Kim, J. A. Elle, A. B. Sushkov, G. S. Jenkins, H. M. Milchberg, M. S. Fuhrer, and H. D. Drew, *Nat. Nanotechnol.*, 2012, **7**, 472–478.
127. X. Gan, K. F. Mak, Y. Gao, Y. You, F. Hatami, J. Hone, T. F. Heinz, and D. Englund, *Nano Lett.*, 2012, **12**, 5626–5631.
128. R. Mas-Ballesté, C. Gómez-Navarro, J. Gómez-Herrero, and F. Zamora, *Nanoscale*, 2011, **3**, 20–30.
129. K. S. Novoselov, D. Jiang, F. Schedin, T. J. Booth, V. V. Khotkevich, S. V. Morozov, and A. K. Geim, *Proc. Natl. Acad. Sci. USA*, 2005, **102**, 10451–10453.
130. K. F. Mak, C. Lee, J. Hone, J. Shan, and T. F. Heinz, *Phys. Rev. Lett.*, 2010, **105**, 136805.
131. B. Radisavljevic, A. Radenovic, J. Brivio, V. Giacometti, and A. Kis, *Nat. Nanotechnol.*, 2011, **6**, 147–150.
132. H. S. Lee, S.-W. Min, M. K. Park, Y. T. Lee, P. J. Jeon, J. H. Kim, S. Ryu, and S. Im, *Small*, 2012, **8**, 3111–3115.
133. Y. Y. Hui, X. Liu, W. Jie, N. Y. Chan, J. Hao, Y.-T. Hsu, L.-J. Li, W. Guo, and S. P. Lau, *ACS Nano*, 2013, **7**, 7126–7131.
134. Z. Yin, H. Li, L. Jiang, Y. Shi, Y. Sun, and G. Lu, *ACS Nano*, 2011, **6**, 74–80.

135. O. Lopez-Sanchez, D. Lembke, M. Kayci, A. Radenovic, and A. Kis, *Nat. Nanotechnol.*, 2013, **8**, 497–501.
136. K.-K. Liu, W. Zhang, Y.-H. Lee, Y.-C. Lin, M.-T. Chang, C.-Y. Su, C.-S. Chang, H. Li, Y. Shi, H. Zhang, C.-S. Lai, and L.-J. Li, *Nano Lett.*, 2012, **12**, 1538–1544.
137. Y. Zhan, Z. Liu, S. Najmaei, P. M. Ajayan, and J. Lou, *Small*, 2012, **8**, 966–971.
138. M. Fontana, T. Deppe, A. K. Boyd, M. Rinzan, A. Y. Liu, M. Paranjape, and P. Barbara, *Sci. Rep.*, 2013, **3**, 1634.
139. D. J. Late, B. Liu, H. S. S. R. Matte, C. N. R. Rao, and V. P. Dravid, *Adv. Funct. Mater.*, 2012, **22**, 1894–1905.
140. S. Lei, L. Ge, Z. Liu, S. Najmaei, G. Shi, G. You, J. Lou, R. Vajtai, and P. M. Ajayan, *Nano Lett.*, 2013, **13**, 2777–2781.
141. P. Hu, Z. Wen, L. Wang, P. Tan, and K. Xiao, *ACS Nano*, 2012, **6**, 5988–5994.
142. P. Hu, L. Wang, M. Yoon, J. Zhang, W. Feng, X. Wang, Z. Wen, J. C. Idrobo, Y. Miyamoto, D. B. Geohegan, and K. Xiao, *Nano Lett.*, 2013, **13**, 1649–1654.
143. D. J. Late, B. Liu, J. Luo, A. Yan, H. S. S. R. Matte, M. Grayson, C. N. R. Rao, and V. P. Dravid, *Adv. Mater.*, 2012, **24**, 3549–3554.
144. W. J. Yu, Y. Liu, H. Zhou, A. Yin, Z. Li, Y. Huang, and X. Duan, *Nat. Nanotechnol.*, 2013, **8**, 4–10.
145. L. Britnell, R. M. Ribeiro, A. Eckmann, R. Jalil, B. D. Belle, A. Mishchenko, Y.-J. Kim, R. V. Gorbachev, T. Georgiou, S. V. Morozov, A. N. Grigorenko, A. K. Geim, C. Casiraghi, A. H. Castro Neto, and K. S. Novoselov, *Science*, 2013, **340**, 1311–1314.
146. T. Georgiou, R. Jalil, B. D. Belle, L. Britnell, R. V. Gorbachev, S. V. Morozov, Y.-J. Kim, A. Gholinia, S. J. Haigh, O. Makarovsky, L. Eaves, L. A. Ponomarenko, A. K. Geim, K. S. Novoselov, and A. Mishchenko, *Nat. Nanotechnol.*, 2013, **8**, 100–103.
147. L. Britnell, R. V. Gorbachev, R. Jalil, B. D. Belle, F. Schedin, A. Mishchenko, T. Georgiou, M. I. Katsnelson, L. Eaves, S. V. Morozov, N. M. R. Peres, J. Leist, A. K. Geim, K. S. Novoselov, and L. A. Ponomarenko, *Science*, 2012, **335**, 947–950.
148. R. V. Gorbachev, A. K. Geim, M. I. Katsnelson, K. S. Novoselov, T. Tudorovskiy, I. V. Grigorieva, A. H. MacDonald, S. V. Morozov, K. Watanabe, T. Taniguchi, and L. A. Ponomarenko, *Nat. Phys.*, 2012, **8**, 896–901.
149. V. Bouchiat, *Nat. Phys.*, 2012, **8**, 862–863.
150. J. M. Hamm and O. Hess, *Science*, 2013, **340**, 1298–1299.
151. H. Sun, Z. Xu, and C. Gao, *Adv. Mater.*, 2013, **25**, 2554–2560.
152. W. Ren and H. Cheng, *Nature*, 2013, **497**, 448–449.